Higher Levels of the Transmon Qubit

by

Samuel James Bader

Submitted to the Department of Physics
in partial fulfillment of the requirements for the degree of

Bachelor of Science in Physics

at the

MASSACHUSETTS INSTITUTE OF TECHNOLOGY

June 2014

Signature redacted

Author .....
Department of Physics
May 9, 2014

Signature redacted

Certified by .....
Terry P. Orlando
Professor of Electrical Engineering
Thesis Supervisor

Signature redacted

Certified by .....
Simon Gustavsson
Research Scientist
Thesis Co-Supervisor

Signature redacted

Accepted by .....
Professor Nergis Mavalvala
Senior Thesis Coordinator, Department of Physics

Higher Levels of the Transmon Qubit

by

Samuel James Bader

Submitted to the Department of Physics
on May 9, 2014, in partial fulfillment of the
requirements for the degree of
Bachelor of Science in Physics

Abstract

This thesis discusses recent experimental work in measuring the properties of higher levels in transmon qubit systems. The first part includes a thorough overview of transmon devices, explaining the principles of the device design, the transmon Hamiltonian, and general Circuit Quantum Electrodynamics concepts and methodology. The second part discusses the experimental setup and methods employed in measuring the higher levels of these systems, and the details of the simulation used to explain and predict the properties of these levels.

Thesis Supervisor: Terry P. Orlando
Title: Professor of Electrical Engineering

Thesis Supervisor: Simon Gustavsson
Title: Research Scientist

Acknowledgments

I would like to express my deepest gratitude to Dr. Simon Gustavsson, who, over the last several months, has been a brilliant supervisor, a role-model researcher, and solid friend to me. I have learned a great deal from Simon, not only about superconducting qubits and microwave techniques, but about how one should conduct research. I am still constantly amazed by his facility in leaping between five levels of experimental abstraction when trouble-shooting, and his foresight in building and refining the software and practices which make the lab function. His cleverness in the face of technical difficulties and ability to keep the big picture in sight has taught me a lot, and I have to say, we made a pretty good team.

Thank you to Professor Terry Orlando for agreeing to take me on for a thesis project, even though I was entirely new to the subject. His course on Applied Superconductivity, one of the most enjoyable classes I have ever had, is what started me down this research path; he taught me most of what I know, and what an adventure it was. With his legendary friendliness, joviality, and warmth, Terry is always a pleasure, both to learn from and to work with.

Thanks also to Dr. William Oliver from MIT Lincoln Laboratory, whose insights often gave me interesting new directions to explore. Will's conviviality, awe-inspiring scientific acuity, and smooth leadership always made me look forward to the weekly group meetings.

Thank you to Michael Peterer in the University of Oxford Department of Physics. He and Simon did much of the initial ground-breaking experimental work before I joined the group. My work on the simulations, and the reason I joined this project, was originally motivated by trying to explain the strange phenomena Michael noticed, and much of my experimental work has involved attempts to improve the quality of data from measurements he made. His role in this cannot be understated.

Thanks also to the rest of the Orlando group, Dr. Archana Kamal, Dr. Xiaoyue Jin, and Dr. Fei Yan, for helpful discussions and for making me feel welcome.

Thanks to my parents, Larry Bader and Peggy Warner, for always supporting me in my education, and for their love and advice at every turn. A special thank you to my sister, Lexy

Bader, for supplying me with fruit and sustenance to battle pneumonia over the weekend before this thesis was due, and for always being there for me.

I am incredibly grateful to every one of the above, without whom this thesis would not have been possible.

Contents

Chapter 1

Introduction

Quantum information processing is one of the most thrilling prospects to emerge from the interaction of physics and computer science. In recent decades, scientists have transitioned from merely observing microscopic systems to actually controlling those same systems on the scale of individual quanta, and the future of information processing based on these techniques will revolutionize the computing industry. This paper will explore one exciting candidate realization of this means of computing, the superconducting "transmon", and extend the discussion beyond the typical two-level "qubit."

Why quantum computers?

Quantum computers leverage the quantum phenomena of superposition and entanglement, which together allow for massively parallel operations in an exponentially enlarged computational space [1]. Several famous algorithms have been proposed to capitalize on these advantages. For instance, the Shor factoring method is exponentially faster than known classical algorithms at solving a problem whose difficulty underlies much of modern cryptography, and the Grover search method provides a square-root speed-up to the ubiquitous procedure of (unsorted) database searching. While these algorithms will impact matters ranging from general computing to information security, the most important use of quantum computers may actually be the simulation of other complex quantum systems [2]. Modern

research, in subjects ranging from medicinal drug discovery to high-temperature superconductivity, requires simulating systems which classical computers are inherently inefficient at modeling. These fields stand to benefit greatly from the quantum computational power boost.

The qubit

Many schemes [1] have been proposed to implement the quantum bit ("qubit") of such a computer, most commonly relying on *microscopic* quantum systems such as nuclear or electronic spins, photon polarizations, or electronic levels in trapped ions or in crystal defects. One approach, however, utilizes the *macroscopic* quantum phenomena of superconductivity. This brings about two major advantages. First, these systems–unlike an atom which is fixed by nature–can be engineered to desirable specifications. Second, due to their size, they can be built via the familiar, scalable micro-fabrication methods of the conventional semiconductor industry, which is vital if these qubits are to be manufactured into arbitrarily large computers. The Achilles heel of superconducting qubits has always been short coherence times–the coherence time is essentially how long the system shows coherent quantum behaviour, before damping and dephasing drain the information away. Because of their macroscopic size, superconducting circuits couple strongly to their surroundings in comparison to well-isolated microscopic systems. Although this once presented a seemingly unsurmountable obstacle, researchers have steadily discovered and eliminated more sources of noise with remarkably clever designs, and qubit coherence times have lengthened by several orders of magnitude [3] within the last decade, making superconducting systems an increasingly promising choice of qubit.

A qubit must simultaneously satisfy a difficult set of constraints in order to have any utility. It must stay coherent (on its own or more likely with error correction) on a timescale long enough to apply computations. Thus it cannot couple too much to the environment, but it must couple strongly to a classical system in some controllable way, so that it can be manipulated quickly. To make a computer, it also has be to be possible to address *only* the

qubit transition between whichever levels store information, without exciting other levels. A harmonic oscillator, for instance, would not work because all levels are uniformly spaced, so a pulse which excites the first transition would also excite the second (and third and any others). It also has to be possible to controllably entangle multiple qubits together in order to perform any non-trivial computation.

The transmon

Acheiving these criteria in a variety of systems has been a tremendous scientific effort, and only in the last several years have superconducting systems become plausible competitors. First proposed in 2007 [4], the transmon and its descendants are a leading architecture for superconducting qubits, with experimental coherence times of $\sim$ 100 μs[3], demonstrated multiqubit entanglement [5], [6], and a transmission line structure which naturally lends itself to incorporation with various interesting Circuit Quantum Electrodynamics (CQED) proposals, e.g. [7]. The theory section of this paper will discuss the physical elements involved in the design of a transmon qubit, from its basis in the capacitively shunted Cooper Pair Box, to the techniques of coupling with a transmission line resonator, to protocols for performing quantum operations upon the system. The first two chapters will rationalize the architecture of the system, and the third will discuss how such a design can be used to implement computation.

Beyond the qubit

Although most of the quantum computation literature deals with ideal two-level systems, the transmon Hilbert space, as discussed in the theory section, does inevitably contain higher levels. These are not necessarily a curse, as there have been recent experiments and proposals for quantum computation making use of the advantages of larger computational spaces [8]–[10]. The experimental section of this thesis will explore the accessible higher levels of a transmon, locating their frequencies and determining their coherence properties. This will test the transmon Hamiltonian and provide the basic values necessary for running multi-level

computation schemes on a transmon system.

Assumptions of the Reader

This work assumes that the reader has a prior background in superconductivity and Josephson phenomena, on the level of an introductory text such as [11].

Part I

Theory

Chapter 2

Qubit Architecture

The transmon is a cleverly optimized architecture which simultaneously balances many of the mentioned requirements for successful qubit. Since the transmon is built up from a modified version of the conceptually simpler "Cooper Pair Box" qubit, our discussion will begin there and then steadily add the new features, a capacitive shunt and a coupled transmission line, until the entire design has been rationalized.

2.1 Cooper Pair Box

The Cooper Pair Box (CPB) is the prototypical "charge" qubit–that is, a qubit wherein the charge degree of freedom is used for couping and interaction. Coherent quantum oscillations were first demonstrated in this system in the late 90's [12], [13]. In its most basic form, the CPB consists of a superconducting island into which Cooper pairs may tunnel via a Josephson junction. Such a structure is shown in Figure 2-1a. In order to apply the quantum theory of circuits and understand how such a structure can demonstrate quantum coherence, the structure of Figure 2-1a can be translated into the schematic shown in Figure 2-1b, which is formally treated below.

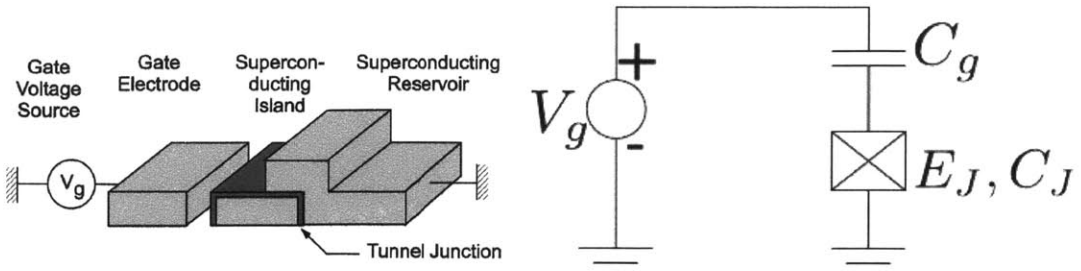

(a) (b)

Figure 2-1: **(a)** A prototypical implementation of the Cooper Pair Box, containing a superconducting "island" which is electrically connected to the rest of the circuit only by a Josephson tunneling current. The light grey material is a superconductor (e.g. Aluminum) and the dark junction an insulator (e.g. Aluminum Oxide). Reprinted from [14]. **(b)** Translation into a circuit schematic, where the crossed box symbolizes a Josephson junction. The superconducting island has been highlighted red.

2.1.1 Classical Hamiltonian

The Hamiltonian for this circuit is derived in Appendix A.1 under a standard classical procedure.

$$\mathcal{H} = \frac{(Q_J - C_g V_g)^2}{2C_\Sigma} - E_J \cos\delta$$

where $C_\Sigma = C_g + C_j$ is the total capacitance of the island, Q_J is the charge in the island, and δ is the superconducting phase across the junction.

The first term of the Hamiltonian represents the capacitive/charging energy and the second term is the Josephson inductive energy. Note that the charging term depends on the excess charge *minus an offset* which is controlled by the gate voltage.

We will rewrite this expression by naming several useful quantities. The charging energy scale is set by $E_C = e^2/2C_\Sigma$ (many authors differ in a factor of four, but this convention seems to dominate within the transmon literature). And we rephrase the charge variable in terms of $n = Q_j/(2e)$, the number of Cooper pairs inside the island:

$$\mathcal{H} = 4E_C\,(n - n_g)^2 - E_J \cos\delta$$

where $n_g = C_\Sigma V_g/(2e)$ is called the effective offset charge. This form of the Hamiltonian,

which highlights the relevant energy scales in the problem, will be used throughout the paper.

Split Junction

In practice [13], the schematic is only slightly more complex that what we have just treated: the qubit is typically implemented with *split* Cooper Pair Box. Two parallel junctions replace the single junction, as shown schematically in Figure 2-2. However, it can be shown that this pair merely creates an effective single junction, for which the Josephson energy can be tuned *in situ* by putting the magnetic flux through the pair [14]. This is vital for two reasons. First, it implies that the Hamiltonian which we derived for the prototypical CPB also applies to the split-CPB system. And second, the ability to tune the qubit parameters (and thus its frequency) will be useful for implementing quantum gates in Sec 3.

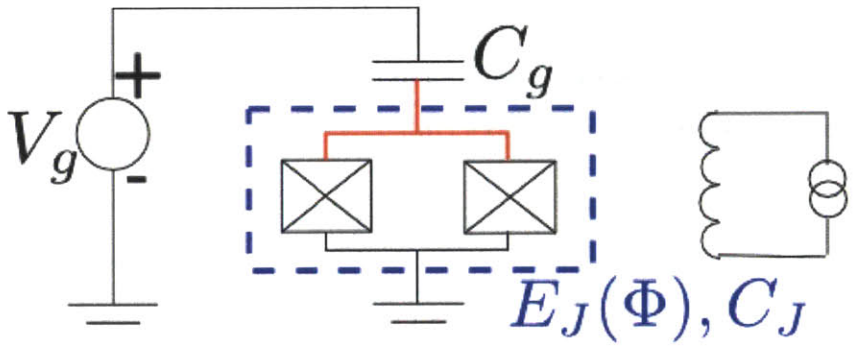

Figure 2-2: The split pair forms an effective junction whose Josephson Energy E_J can be tuned by application of an external flux Φ from a bias line.

2.1.2 Quantized Hamiltonian

Quantization at the sweet spot

We will now quantize the CPB circuit with the commutation relation $[n, \delta] = i$, as described in Appendix B, and write the Hamiltonian in a familiar form. When the energy scale for the capacitive charging of the island is dominant (i.e. $E_C \gg E_J$), the natural choice of basis states for the system, $\{|n\rangle\}$, is labelled by the number of excess Cooper pairs in the island. Since the CPB is generally operated in this regime–hence the name "charge qubit"–much

intuition can be gleaned by working in the basis of charge eigenstates (as introduced in Appendix B).

Using (B.1), we quantize in this basis:

$$\mathcal{H} = 4E_c(n - n_g)^2 \left|n\right\rangle \left\langle n\right| - \frac{E_J}{2}\left(\sum_n \left|n+1\right\rangle \left\langle n\right| + \left|n-1\right\rangle \left\langle n\right|\right) \tag{2.1}$$

Now, how can we get a single pair of qubit levels well-separated from the others? The CPB is typically biased at the "sweet spot" such that $n_g \approx 1/2$: this makes the charging term degenerate with respect to the states $\{\left|0\right\rangle, \left|1\right\rangle\}$, and that degeneracy is broken by the Josephson term. With $E_C \gg E_J$, other levels will be far separated (order of E_C) and we can focus on those two states as our qubit. If $n_g = 1/2$, then $\mathcal{H}$ is off-diagonal, so the eigenstates would be $\left|\pm\right\rangle = \frac{1}{\sqrt{2}}\left(\left|0\right\rangle \pm \left|1\right\rangle\right)$, with a splitting of E_J.

Rotating into this $\left|\pm\right\rangle$ basis, the Hamiltonian acting upon this subspace can be rewritten in a familiar form using the Pauli matrices [15]:

$$H = E_z\sigma_Z + X\sigma_X \tag{2.2}$$

where $E_z = E_J/2$, and $X = 4E_C(n_g - \frac{1}{2})$. This form lets us view the system in analogy to the standard NMR Hamiltonian.

How to control and readout

The NMR Hamiltonian is a frequently used picture for quantum computation. Note that X in Eq 2.2 is controlled by the gate voltage V_g, and that oscillating the parameter X of a CPB system is mathematically analogous to sending a transverse pulse of magnetic field to an NMR nucleus. Thus by supplying an oscillating gate voltage about the sweet spot, one can apply the σ_x gate to a CPB qubit. And by simply waiting (or, in the rotating-frame picture, adjusting the phase of the pulse programmer) one applies a σ_z gate.

Readout could be performed by rotating the system to a charge basis and then classically measuring the charge in the island, via, for instance, a single-electron transistor [12], [13].

Alternative methods include measurement via quantum capacitance [16], or resonator-based readout [17]. The last option is the one which will be important to this work, so further discussion of qubit control and readout will be come after the discussion of resonator coupling with Circuit QED.

Energy Spectrum

While the charge basis gave us an intuitive picture of the qubit eigenstates of the CPB Hamiltonian, it is also worth mentioning that the full set of energies can be solved for exactly in the phase representation (again see Appendix B). In this representation, the Hamiltonian becomes

$$H = 4E_C \left(-i\frac{\partial}{\partial \delta} - n_g \right)^2 - E_J \cos\delta$$

Note that this is the same form as the effective Schrodinger equation which is solved to find the energy eigenstates of a particle an a periodic potential, with n_g taking the role of the Bloch wavevector (see Appendix C.1), so it is no surprise that the resulting energy spectrum, when plotted as a function of n_g, looks like a band structure. In this particular case–a cosine potential–the solution is known in terms of the Mathieu functions: the full energy spectrum is given by

$$E_k = 4E_C \times \mathcal{M}_A[(k+1)\%2 + 2(-1)^k n_g, -2E_J/E_C]$$

where $x\%2$ indicates the remainder when x is divided by 2, and $\mathcal{M}_A(r,q)$ is the characteristic value for even Mathieu functions with characteristic exponent r and parameter q, see [15]. The energies are plotted in Figure 2-3a for the $E_C \gg E_J$ case discussed.

One feature worth noting in the spectrum is that the energy levels for the charge qubit are strongly dependent on the offset charge n_g, which makes the qubit dangerously sensitive to charge noise from the environment: low-frequency charge fluctuations (the ubiquitous "$1/f$ noise") will perturb the transition frequency and whittle away phase coherence of the qubit. This noise sensitivity is reduced by operating at the "sweet spot" $n_g = 1/2$ where the energy is first-order independent of offset charge [18]. Intuitively, the levels at the sweet

spot are both equal superpositions of the two charge eigenstates, so first-order perturbation theory won't distinguish the two. But even with this intelligent biasing, charge noise is still a dominant decoherence mechanism [4].

However, note that in Figure 2-3b, where E_J/E_C has been increased such that the charging term no longer dominates, the charge sensitivity of the qubit is intuitively diminished. The trade-offs involved in this suggestive option will be discussed in the next section, leading us to a simple redesign of the qubit.

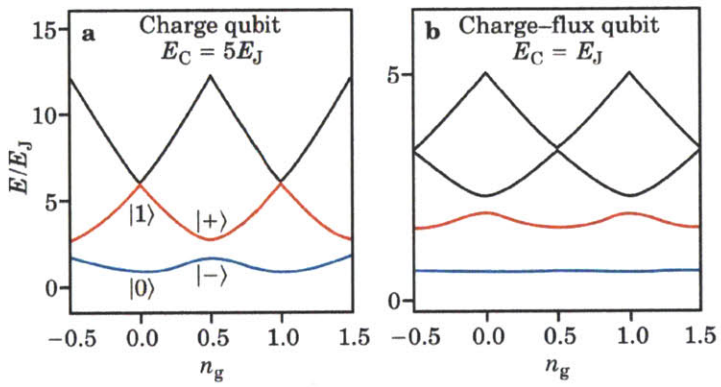

Figure 2-3: Energy levels for the CPB as a function of the effective offset charge. In (a), where E_C is sufficiently greater than E_J, there is a sweet spot such that the bottom two levels form a well-isolated qubit with basis states $\{|\pm\rangle\}$. (b) Where $E_C \sim E_J$, charge and flux degrees of freedom are both important. Reprinted from [18].

2.2 Capacitively-shunted CPB

This section will more thoroughly explore the benefits of moving beyond the charge qubit into a regime of high E_J/E_C, by capacitively shunting the Cooper Pair Box. The first order of business is to continue the discussion from the previous section to more rigorously examine how the properties of the qubit depend on this ratio.

2.2.1 The ratio E_J/E_c

In the discussion thus far, we have taken E_C to dominate over E_J, as is appropriate for a charge qubit. However, the (exact) energy spectrum given in the previous section does not depend on any such approximation, and this solution raises a trade-off to be considered for the parameter E_J/E_C. The choice of this ratio affects both the device's anharmonicity and its sensitivity to charge noise.

As discussed, the low E_J/E_C limit creates a spectrum like that in Figure 2-3a, which is highly dependent on the value of n_g, and thus susceptible to enivronmental charge noise. To combat charge noise, one would consider raising the ratio to reduce the influence of the charging term. This produces what is known as a charge-flux qubit.

But a low E_J/E_C is what provides high anharmonicity. As discussed in the charge basis, this regime gives rise to a spectrum in which the energy depends quadratically on the quantum number n. This quadratic dependence means that the energy difference between the first and second levels is much tighter than that between the second and third, and so on up the ladder; this can be seen in Figure 2-3a. Since these two transitions have different frequencies, they can be selectively addressed by pulses. But if E_J/E_C were large, as in Figure 2-3b, then the Hamiltonian begins to approach a harmonic oscillator (this will be shown below), and the energy levels adjust toward a relatively uniform spacing, and eventually will not be selectively addressable. So the requirement of anharmonicity favors the purely charge qubit we've discussed.

So the necessity of anharmonicity biases the experimenter toward low E_J/E_C, but the desire to lower charge noise suggests high E_J/E_C. We will therefore examine how each property depends on this vital ratio, following [4], so as to determine whether some middle ground exists.

Anharmonicity

As E_J/E_C is raised, the $\cos\delta$ term dominates, and, falling back upon the picture of a particle in a periodic potential (see Appendix C.1), the atomic wells become increasingly deep and

the states localized within each well become increasingly decoupled from one another. The energies will thus depend on the shape of the potential only near the bottom of the well at $\delta = 0$, where $\cos\delta \approx 1 - \delta^2/2 + O(\delta^4)$. So, for large E_J/E_C, the anharmonicity comes entirely from the higher-order terms in $\cos\delta$, and the problem reduces to perturbing a harmonic oscillator. This is analyzed in depth in Appendix C, and the result is that the anharmonicity, quantified as the relative difference between the first two transition frequencies, falls off with a simple algebraic dependence on E_J/E_C:

$$\frac{E_{12} - E_{01}}{E_{01}} \approx -(8E_J/E_C)^{-1/2}$$

Charge dispersion

On the other hand, the dependence of the levels on n_g, the "charge dispersion," does not arise from a simple perturbation of the harmonic oscillator. We can argue that this property actually depends on the height of the potential far from the high-amplitude region of the wavefunction.

Again considering the periodic potential analogy of Appendix C.1, the case of deep, decoupled wells is addressed by the tight-binding model of band theory. In tight-binding, the energy levels of an individual well are assumed to be known, but the coupling between neighboring wells pertubs this by the addition of tunnelling matrix elements, which create the bandstructure. Tunneling is, as usual, exponentially suppressed by the height of the potential barrier in between the wells, where the wavefunction is small.

Translating back to the CPB, the "band structure" is n_g dependence, and the "potential barrier height" is determined by E_J/E_C. So, in high barriers, the effects of the band structure, and thus any dependence on n_g, are exponentially suppressed by large E_J/E_C. This fact is the key to understanding why the a higher E_J/E_C is desirable: the charge dispersion decays exponentially fast, while the anharmonicity, preserved by the higher-order terms of the cosine, only slowly decreases.

Shunting the CPB

From the Section 2.1.1, recall that the charging energy E_C is inversely related to the junction capacitance. The standard way to increase E_J/E_C is thus to add a large "shunt" capacitance across the Josephson junction (as shown in Figure 2-4). Since C_B adds in parallel with C_J, but is much larger, C_J can just be absorbed into C_B to simplify the algebra. This reduces the Hamiltonian of the new circuit back to the CPB Hamiltonian but with $C_J \to C_B$, so all of the previous discussion holds. In practice with such a qubit, E_C might be in the hundreds of MHz and E_J in the tens of GHz [5], [6].[1]

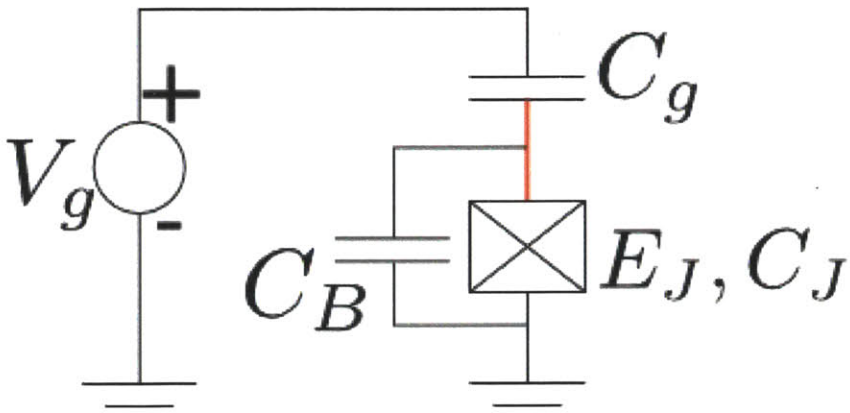

Figure 2-4: A large capacitor is added across the junction to reduce E_C.

The first question to address for this modification must be how to couple to such a qubit for control and readout. The electrostatic charge-based methods mentioned in Section 2.1.2 will not be effective for our modified qubit, whose Hamiltonian is no longer dominated by charging energy. But the next section will rescue the new design by exploring the physics of resonator-based based readout alternative for this capacitively shunted CPB, which is the last ingredient to making a transmon qubit.

[1]Note: as discussed, E_J is a tunable parameter for the split Josephson junction, so both of [5], [6] list the value as $E_J^{\max}$.

Chapter 3

Circuit QED

We previously discussed means of coupling directly to a CPB qubit using its charge degree of freedom for control and readout. However this section will introduce an indirect means of interacting with the qubit: coupling the circuit to a transmission line resonator and interacting only with the resonator itself. The scheme is often referred to as Circuit Quantum Electrodynamics (Circuit QED), analogous to the study of confined atom-light interactions in Cavity QED.

The advantages of this approach are many-fold. First, it will provide a controllably isolated environment for the qubit, inhibiting spontaneous decay by a means similar to the Purcell effect in Cavity QED. Second, it will allow non-destructive measurements (i.e. measurements which do not reset the qubit). And third, it will suggest a simple way to couple multiple qubits together. All of these will be discussed in depth once we have built up a Cavity QED framework for the physics.

3.1 Vocabulary of Cavity QED

Cavity QED describes the interactions between atoms and quantized electromagnetic fields in a cavity; as this is already a rich research field, the literature of Circuit QED has adopted much of its preexisting jargon and intuition [19]. This section will introduce the basic lan-

guage of Cavity QED and clarify the analogy with its superconducting circuit manifestation.

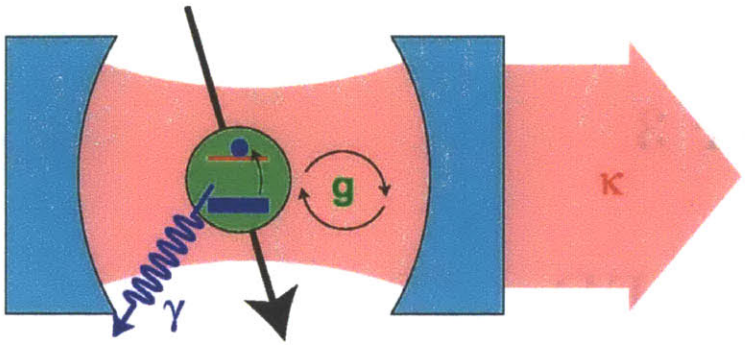

Figure 3-1: As an atom passes through the cavity, it couples (with strength g) to the electromagnetic fields of a nearby cavity mode. Near resonance, this interaction can be intuited as absorbing photons to excite the atom and reemitting photons to deexcite the atom. Also depicted are losses from interaction with other modes (γ) and from imperfect cavities (κ). These losses will be neglected for the moment. Modified from [19].

3.1.1 Jaynes-Cummings Hamiltonian

The prototypical system of Cavity QED is the coupling between an atom and a cavity when an atomic transition frequency is near a cavity mode. Here we will "derive by declaration" the Jaynes-Cummings Hamiltonian modeling this interaction. A more rigorous derivation of this standard Hamiltonian can be found in many sources [20], but our purpose here is mainly to build up an analogy for Circuit QED, wherein we will derive a similar Hamiltonian by a more thorough circuit analysis.

The coupling depicted in Figure 3-1 is between an atomic transition of frequency Ω and a single mode of the cavity at frequency ω_r. The atom is approximated by a two-level system $\{|g\rangle, |e\rangle\}$ and enters the Hamiltonian through the Pauli matrices $H_{\text{atom}} = \frac{\hbar\Omega}{2}\sigma_z$. The cavity mode is described by a harmonic oscillator with ladder operators a and $a^\dagger$, so it appears in the Hamiltonian via a number operator $H_{\text{cavity}} = \hbar\omega_r(a^\dagger a + \frac{1}{2})$.

Finally, the atomic dipole moment couples with the electric fields of the cavity mode. The electric field is analogous to the position operator of the harmonic oscillator, so it is

proportional to $\mathcal{E}_{\rm rms}(a+a^\dagger)$, where $\mathcal{E}_{\rm rms}$ is the root-mean-square electric field of a single cavity photon. The dipole moment D of the atom is off-diagonal in the Pauli basis since atomic energy eigenstates themselves have no dipole moments; thus $D = d\sigma_x = d(\sigma^+ + \sigma^-)$ where $d = |\langle g|D|e\rangle|$. The interaction is then $H_{\rm int} = \mathcal{E}_{\rm rms} d(a+a^\dagger)(\sigma^+ + \sigma^-)$. Using the rotating wave approximation [20] to eliminate the quickly oscillating terms, and collecting the prefactors into a "couping strength" $g = \mathcal{E}_{\rm rms} d/\hbar$, we have $H_{\rm int} = \hbar g(a\sigma^+ + a^\dagger\sigma^-)$. Putting this all together we have the standard Jaynes-Cummings Hamiltonian:

$$H_{\rm JC} = \frac{\hbar\Omega}{2}\sigma_z + \hbar\omega_r(a^\dagger a + \frac{1}{2}) + \hbar g(a\sigma^+ + a^\dagger\sigma^-)$$

This Hamiltonian will describe the dynamics well if the losses we've neglected (see Figure 3-1) are negligible, that is, the other cavity modes are far detuned from the atomic transition and the leakage of the cavity is small. This regime $g \gg \kappa, \gamma$ is known as "strong coupling."

To set the scales and get a sense for the difficulty of strong coupling [19], Cavity QED is generally implemented [21] with optical transitions (e.g. 350 THz in Cesium) or microwave transitions (e.g. 51 GHz in highly excited "Rydberg" atoms), and the dipole moment is fixed by the atom (so about one ea_0 or up to about 10^3 ea_0, respectively). The resulting values of g are $110 \times 2\pi$ MHz or $24 \times 2\pi$ kHz. What is important to note is that the timescale $2\pi/g$ for coupling effects is longer than the transition timescale by a factor of more than a million. So in order to see coherent effects of the atom-cavity interaction, the cavities must be extremely high quality ($Q \sim 10^7, 10^8$). With these limits, a typical cavity lifetime is only a few times longer than the coupling timescale (at least for low photon numbers). So, in order to see coherent behavior at the single photon scale, Cavity QED has little margin for imperfections.

3.1.2 Effects of the coupling: resonant and dispersive limits

Diagonalizing the above Jaynes-Cummings Hamiltonian yields a set of "dressed state" solutions which mix the atomic eigenstates with the cavity eigenstates. The ground state is

$|g,0\rangle$, that is, an unexcited atom in an empty cavity. The excited states are, following [19]:

$$\overline{|+,n\rangle} = +\cos\theta_n\,|e,n\rangle + \sin\theta_n\,|g,n+1\rangle$$
$$\overline{|-,n\rangle} = -\sin\theta_n\,|e,n\rangle + \cos\theta_n\,|g,n+1\rangle$$

with the mixing angle θ_n

$$\theta_n = \frac{1}{2}\tan^{-1}\left(\frac{2g\sqrt{n+1}}{\Delta}\right)$$

where Δ is the detuning $\Omega - \omega_r$. And the energies are given by

$$E_{\overline{\pm,n}} = (n+1)\hbar\omega_r \pm \frac{\hbar}{2}\sqrt{4g^2(n+1)+\Delta^2}, \quad E_{g,0} = -\frac{\hbar\Delta}{2}$$

There is much intuition to be gained by examining the limiting cases of Δ. If $\Delta \ll g$, that is, the atom is resonant with the cavity, then photon absorption and emission are energy-conserving. Mathematically, $\theta_n = \pi/4$, and the eigenstates are equal combinations of excited atoms with n photons and de-excited atoms with $n+1$ photons. The spectrum is a set of doublets which are split by the coupling energy, as shown in Figure 3-2a.

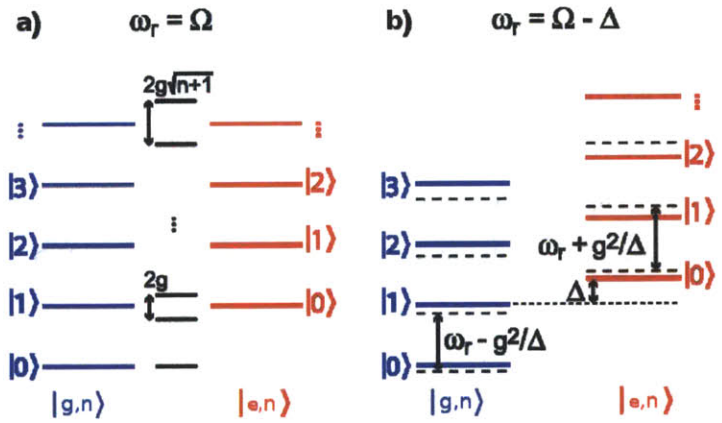

Figure 3-2: Levels of the Jaynes-Cummings Hamiltonian in the resonant and dispersive limits. (a) On resonance, the spectrum can be view as a set of dressed-state doublets split by the coupling. (b) Detuned from resonance where the unperturbed eigenstates are approximately valid, the coupling effectively just shifts the cavity frequency in a manner dependent on the atom's state. Reprinted from [19].

Specifically, an excited atom is not an eigenstate of the combined system: if an initially excited atom is placed into an initially empty cavity, the system is in an equal superposition of the states in the lowest doublet in Figure 3-2(a), and will oscillate with characteristic frequency $2g$ between $|e,0\rangle$ and $|g,1\rangle$. That is, the excitation coherently transfers back and forth between the atom and the electromagnetic modes of the cavity. This process is known as "Rabi flopping" (and $2g$ is the "Rabi frequency").

On the other hand, if $\Delta \gg g$, which is known as the *dispersive* regime, then the eigenstates are nearly those of the unperturbed Hamiltonian:

$$\overline{|+,n\rangle} \approx |e,n\rangle + \frac{g\sqrt{n+1}}{\Delta}|g,n+1\rangle \tag{3.1}$$

$$\overline{|-,n\rangle} \approx |g,n+1\rangle - \frac{g\sqrt{n+1}}{\Delta}|e,n\rangle \tag{3.2}$$

In this limit, we can adiabatically eliminate [22] the coupling, via the unitary $U = \exp\left[\frac{g}{\Delta}(a\sigma^+ + a^\dagger\delta^-)\right]$. The effective Hamiltonian becomes (to second-order in g/Δ)

$$\begin{aligned} UHU^\dagger &\approx \hbar\omega_r a^\dagger a + \frac{\hbar}{2}\left[\Omega + 2\frac{g^2}{\Delta}\left(a^\dagger a + \frac{1}{2}\right)\right]\sigma_z \\ &= \hbar\left[\omega_r + \frac{g^2}{\Delta}\sigma_z\right]a^\dagger a + \frac{\hbar}{2}\left[\Omega + \frac{g^2}{\Delta}\right]\sigma_z \end{aligned} \tag{3.3}$$

This Hamiltonian is written in two different ways to emphasis two interpretations. The first form is familiar from atomic physics, and can be viewed as a photon-number-dependent shift of the atomic frequency (a Stark/Lamb shift). The second form, which will be more useful to us, combines the Stark term with the cavity frequency to view this coupling as a shift of the cavity frequency by an amount dependent on the atomic state. That is, if the atom is in $|e\rangle$, then the cavity frequency is $\omega_r + g^2/\Delta$; if the atom is in $|g\rangle$, then the cavity frequency is $\omega_r - g^2/\Delta$. This dispersive limit can be seen in Figure 3-2b.

3.1.3 Purcell Effect

Spontaneous emission, the eventual decay of any excited energy level in an atom, is often taken as an essential feature of light-matter interaction, endowing atomic levels with "natural" linewidths and decay rates. But, as the above discussion shows, the presence of a cavity fundamentally changes the interaction between an atom and the electromagnetic fields by quantizing the modes available for coupling. If a cavity is resonant with the atom, then the atom can emit and reabsorb photons coherently. Alternatively, if the atom is far detuned from any cavity mode, its eigenstates are very nearly the eigenstates of the system.

The rate at which an atomic level decays is proportional (by Fermi's golden rule) to the density of states of the local electromagnetic field at that atomic frequency. But the mode quantization enforced by a cavity redefines the density of states available to the atom, increasing it in the case of resonance or diminishing it in the case of far detuning. By this channel, the cavity can enhance or reduce the spontaneous emission rate of an atom [23], [24] in what is known as the Purcell effect.

The notion that the cavity shapes the local electromagnetic environment, and thus the lifetime of the atomic excitations, is very suggestive for our mission of building qubits with long-lasting coherent excitations. We will now consider how to realize this, and the other Cavity QED features discussed, in a superconducting system.

3.2 Translating into Circuit QED

In the simplest Circuit QED approach (hereafter CQED), the cavity is replaced by a 1-D transmission line resonator and the atom is, not surprisingly, replaced by superconducting qubit, as shown in Figure 3-3. With this addition, we have reached our objective: the capacitively shunted Cooper Pair Box embedded in a transmission line resonator is known as a transmon qubit. Although we will work off the analogy of the previous section there are several quantitative differences to discuss first.

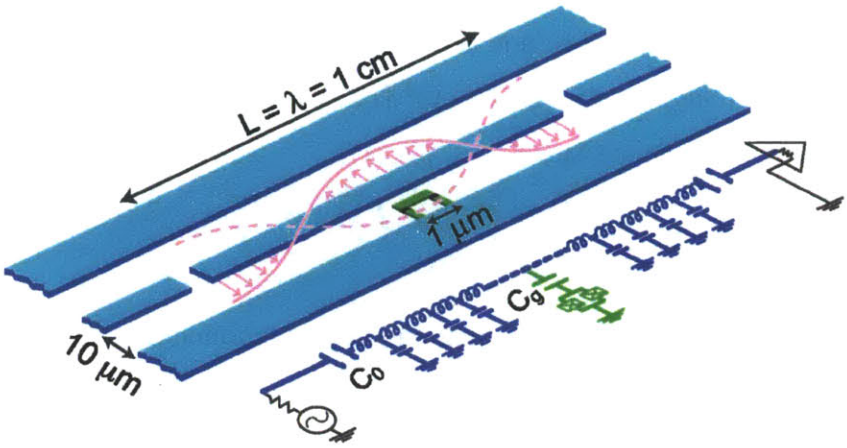

Figure 3-3: Circuit QED uses a transmission line "cavity" and a superconducting qubit as the "artificial atom." The resonator is formed by the capacitive gaps in the center trace of the transmission line, and the outer two traces are ground. Here the qubit is placed at the middle of the resonator to couple to the strong electric fields at the antinode of the second mode. Reprinted from [19].

3.2.1 Why Circuit QED is *easier* than Cavity QED

As before, the coupling is between the electric fields of the cavity and the dipole moment of the "artificial atom" [19], which has a transition tuned to a few GHz. However, since the "atom" is now macroscopic, its dipole moment (which essentially corresponds to moving one Cooper pair across a qubit of dimensions in the microns) is four orders of magnitude greater than that of an optical transition, or about twenty times greater than that of a Rydberg atom. Furthermore, a 1-D resonator (with a width of $\sim$10 microns, as shown in Figure 3-3) offers a much smaller volume of confinement for electromagnetic fields (on the order of 10^{-5} cubic wavelengths) than do 3-D cavities. This increases the root-mean-square electric field strength that corresponds to a single quanta by about two orders of magnitude versus 3-D microwave cavities.

Together these advantages give CQED systems high Rabi frequencies (about 100 MHz) comparable to those of optical atom implementations, but with low transition frequencies (say 10GHz) comparable to those of microwave atom implementations. Since the coupling time scale is only about a hundred times the cavity frequency, the exceedingly high-finesse

resonators used for Cavity QED are not necessary. In fact, although transmission line resonators have been demonstrated with $Q \sim 10^6$ [19], researchers often opt for lower quality cavities to increase measurement speed, e.g. [5], [17].

3.2.2 Circuit QED Hamiltonian

Near the resonant frequency of the transmission line, we can model the line as a lumped LC circuit [17], [19]. In this model, the effective circuit corresponding to Figure 3-3 is given by the schematic in Figure 3-4.

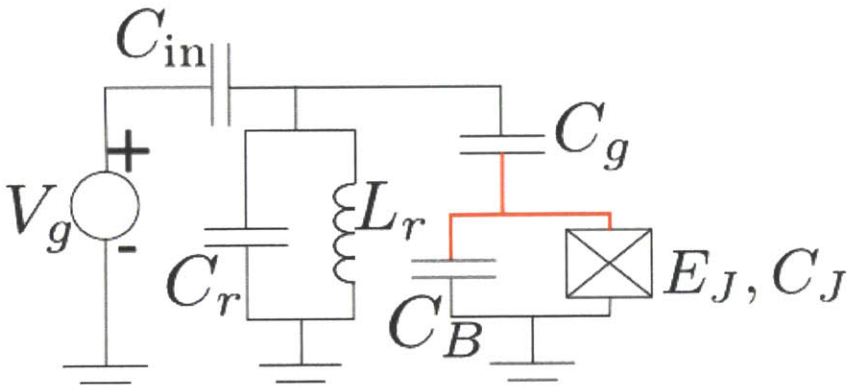

Figure 3-4: Effective circuit for the Transmon.

Using the lumped LC model for the microwave component of the gate voltage V_g, the Hamiltonian of the above circuit is found in Appendix A.2:

$$\begin{aligned}\mathcal{H} = \quad & \frac{\phi_r^2}{2L_r} + \frac{Q_r^2}{2C_r} \\ & + \frac{\left(Q_J - C_g V_g^{\text{DC}}\right)^2}{2C_\Sigma} - E_J \cos\left(\frac{2\pi}{\hbar}\phi_J\right) \\ & + \beta\frac{Q_r Q_j}{C_r} + \frac{C_{\text{in}} Q_r V_g}{C_r}\end{aligned}$$

The first line describes the resonator, the second line describes the CPB, and the third line describes the couplings resonator-to-qubit and resonator-to-gate. The parameter $\beta = C_g/C_\Sigma$ is the voltage divider ratio determining how much of the resonator voltage is seen by the qubit, and V_g^{DC} is the biasing.

To quantize this Hamiltonian and find the Jaynes-Cummings interaction, we rewrite the resonator part with harmonic oscillator ladder operators a and $a^\dagger$, and simplify by defining $V^0_{\text{rms}} = \sqrt{\hbar\omega_r/2C_r}$, the root-mean-square voltage of a single photon in the resonator. For the CPB terms, we assume that the qubit is biased at the sweet spot, restrict to the qubit space, and write the Hamiltonian with the Pauli operators, defined as acting in the qubit eigenbasis. Disregarding the resonator-gate coupling for now, the resonator and qubit Hamiltonian becomes

$$\mathcal{H} = \hbar\omega_r \left(a^\dagger a + \frac{1}{2}\right) + \frac{E_J}{2}\sigma_z - 2e\beta V^0_{\text{rms}} \left(a + a^\dagger\right) n \tag{3.4}$$

The last term is a dipole coupling between the voltage in the resonator and the charge on the qubit. And, as in Cavity QED, the diagonal elements of n vanish (see Appendix C), so we can rewrite this coupling factor in terms of the off-diagonal elements, and employ the rotating-wave approximation to find a Jaynes-Cummings type Hamiltonian:

$$\mathcal{H} = \hbar\omega_r \left(a^\dagger a + \frac{1}{2}\right) + \frac{\hbar\Omega}{2}\sigma_z - \hbar g \left(a^\dagger\sigma^- + a\sigma^+\right) \tag{3.5}$$

where the frequency scales are set by the resonator frequency ω_r, the qubit transition $\Omega = E_J$, and the coupling strength $g = (2e\beta V^0_{\text{rms}}/\hbar)\,\langle e|n|g\rangle$. Note that for the charge-qubit, the matrix element $\langle e|n|g\rangle$ between sweet-spot energy eigenstates is just $1/2$, which reduces the above Hamiltonian to the expressions in [17], [19].

Transmon coupling strength

The matrix elements of n are evaluated in Appendix C, and it is important to register that the coupling strength

$$g = \left(2e\beta V^0_{\text{rms}}/\hbar\right)\left(\frac{E_J}{8E_C}\right)^{1/4}$$

increases slightly with E_J/E_C. In practice, with E_J/E_C of the order 10^2, this increase is not large, within an order of magnitude, but the point is only that the coupling strength is not suppressed by the capacitive shunting. At first glance, this may seem to contradict the

most important result of the previous section, that the charge noise sensitivity of capacitively shunted qubit *decreases* exponentially with E_J/E_C, so the transmon should *not* couple strongly to environmental fields. However, that result was drawn only from considerations of the charge dispersion of the static energy levels; it thus dictates the sensitivity of the qubit to DC charge offsets. That is to say, that noise suppression only describes the response of the qubit to fluctuations of low enough frequency to be considered adiabatic.

So, whereas the last chapter showed that the transmon would be insensitive to $1/f$ charge noise, this new result shows the transmon is also *more* sensitive than the charge qubit to drives near its resonant frequency. This combination is necessary and ideal if the transmon is to serve as a qubit, but where did this boost in coupling strength come from? While the qubit eigenstates of the CPB only involved superpositions of $n = 0$ and $n = 1$, limiting the $\hat{n}$ matrix element to $1/2$, the transmon eigenstates, due to the increased importance of the flux term, will sample a greater range of the charge eigenbasis. Consequently, the transmon is more polarizable, that is, $\langle e|\hat{n}|g\rangle$ involves sums over higher charge eigenvalues than just $n = 0$ and $n = 1$.

Dispersive region with the transmon

As in Cavity QED, the superconducting CQED system can be operated in a dispersive regime wherein the resonator and the qubit are far-detuned, and each effectively just shifts the frequency of the other. With a highly anharmonic CPB qubit, the math is essentially the same as for the Cavity QED dispersive regime. With the more harmonic transmon, however, the second transition also appears in the effective Hamiltonian at the same order [4].

$$H_{\text{eff}} = \hbar\left[\omega_r - \frac{g^2}{2\Delta_2} + \left(\frac{g^2}{\Delta_1} - \frac{g^2}{2\Delta_2}\right)\sigma_z\right] a^\dagger a + \frac{\hbar}{2}\left[\Omega + \frac{g^2}{\Delta}\right]\sigma_z$$

where the Δ_i represent detunings from the first and second transitions. While this can leads to some unusal physics in certain parameter ranges, with dispersive shifts of atypical signs, the end result doesn't change the measurement and control procedures, so, for our purposes, we simply define the dispersive shift $\chi = g^2/\Delta_1 - g^2/2\Delta_2$, and consider the new cavity

frequency ω_r' to be renormalized by a $g^2/2\Delta_2$ term. The Hamiltonian is then

$$H_{\text{eff}} = \hbar\left[\omega_r' + \chi\sigma_z\right] a^\dagger a + \frac{\hbar}{2}\left[\Omega + \frac{g^2}{\Delta}\right]\sigma_z \tag{3.6}$$

There are two main advantages to working in this region. First, the control pulses sent at the qubit frequency will be off-resonant from the transmission line, so the high quality factor of the line does not limit the speed of applying control pulses [17]. Or, alternatively, if a lower quality resonator is used, working in the dispersive regime is necessary because information which flops onto the cavity photons will leak away into the environment [5]. Second, the Purcell effect works in our favor, since the resonator should suppress the local electromagnetic density of states at the detuned qubit frequency, thus inhibiting excited state decay [17].

Now that we have all of the elements of a transmon qubit, the language to describe its interactions with the resonator, and a sense of the rationale for the design and the typical operating regime, what can we do with it?

Chapter 4

Control and Readout Protocol

The preceding two chapters have built up all of the physics necessary to discuss how one can manipulate quantum information using a transmon qubit. Now we will explore the actual protocols for implementing this: how to measure the qubit state, how to control it, and how to entangle multiple qubits together.

4.1 Measurement

Referencing Eq 3.6, the dispersive shift of the resonator frequency dependent on the qubit state provides a natural means of measuring the qubit, by probing the cavity. The two possible transmission profiles are juxtaposed in Figure 4-1, and this contrast suggests two ways that the qubit could be read out.

The most obvious means would be to send a pulse at one of $\omega_r' \pm \chi$. The transmission will be near unity or near zero depending on which energy eigenstate the qubit collapses into. Alternatively, one could send a pulse at the "bare frequency" ω_r' and measure the phase shift of the reflected or transmitted components. As shown in Figure 4-1, the possible phase shifts differ by π, again depending on the qubit state.

The key property of these measurement schemes is that both are valid Quantum Non-Demolition (QND) measurements [17]. That is to say, the measurement collapses the qubit

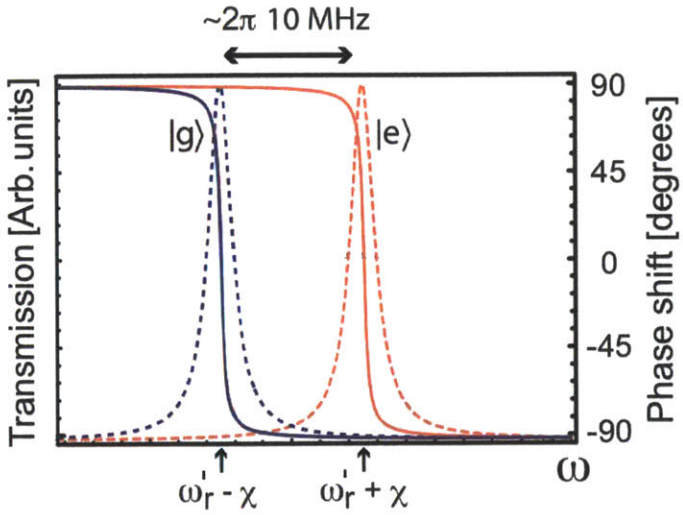

Figure 4-1: The transmission profile of the resonator is shifted to one of two peaks (red or blue) conditioned on the states of the qubit. For drives near $\omega_r' \pm \chi$, the information of the qubit state gets encoded into the transmission probability, and for drives near ω_r', the state gets encoded into the phase shift of the transmitted/reflected photons. Modified from [17]. Note: which peak is $|g\rangle$ or $|e\rangle$ depends on the relative frequency of the qubit and resonator; the above assignment is for $\Omega > \omega_r$.

into some basis state, but thereafter the qubit remains in this state (for times shorter than the excited state decay rate). This is in contrast to, say, measuring the polarization of a photon, afterwhich the photon has been consumed. This superconducting qubit can be measured again immediately afterwards, and the result should be the same.

4.2 Single qubit gates

Whereas driving within χ of the resonator frequency ω_r' results in a measurement, driving at a frequency ω_d far from ω_r' does not leak information about the qubit. As shown in Figure 4-1, the transmission profile for photons off to either side of the peaks does not distinguish between the qubit states. Thus if the qubit and resonator are far-detuned compared to χ, control pulses can be applied at the qubit frequency without measuring the qubit. We will use this convenient fact to apply quantum gates.

4.2.1 Modeling drives

To model single-qubit gates, we note that the effect of a drive is to add a (large, classical) coherent field [25] to the resonator. Mathematically, this just displaces the resonator field operators $a, a^\dagger$ by a classical component α, so that the Jaynes-Cummings Hamiltonian becomes [17]

$$\mathcal{H}_{\text{drive}} = \hbar\omega_r' \left(a^\dagger a + \frac{1}{2}\right) + \frac{\hbar\Omega}{2}\sigma_z - \hbar g\left(a^\dagger\sigma_- + a\sigma^+\right) - \hbar g\left(\alpha^*\sigma_- + \alpha\sigma^+\right)$$

where α can be written in terms of the driving field. Assuming the driving field has constant amplitude ε and frequency ω_d, and dropping transients,

$$\alpha = \frac{\varepsilon}{\omega_r' - \omega_d} e^{-i\omega_d t}$$

Defining the Rabi frequency $\Omega_R = 2\varepsilon g/\Delta_r$, and viewing the system in a frame which rotates with the drive frequency, the effective Hamiltonian for our driven system becomes

$$\mathcal{H}_{\text{rot}} = \hbar\Delta_r \left(a^\dagger a + \frac{1}{2}\right) + \frac{\hbar\Delta_q}{2}\sigma_z - \hbar g\left(a^\dagger\sigma_- + a\sigma^+\right) - \frac{\hbar\Omega_R}{2}\sigma_x$$

where $\Delta_r = \omega_r' - \omega_d$ is the resonator detuning, and $\Delta_q = \Omega - \omega_d$ is the qubit detuning. It is important to realize that the last term allows a classical gate pulse to drive the qubit without any dependence on the resonator. In fact, throughout the manipulations in this section, the resonator will remain empty ($a^\dagger a \approx 0$), since we are driving far from ω_r'.

4.2.2 Applying gates

Since we are working in the dispersive regime, we perform the same adiabatic elimination as in Sec 3.1.2 to find an effective Hamiltonian [17]. Decoupling the qubit and resonator with $U = \exp\left[\frac{g}{\Delta}(a\sigma^+ + a^\dagger\sigma^-)\right]$, and neglecting terms proportional to the occupation of the cavity, we find

$$\mathcal{H}_{\text{eff}} \approx \hbar\Delta_r a^\dagger a + \frac{\hbar}{2}\left(\Delta_q + \frac{g^2}{\Delta}\right)\sigma_z + \frac{\hbar\Omega_R}{2}\sigma_x \tag{4.1}$$

where Δ is still the resonator-qubit detuning. To summarize, this is the effective Hamiltonian of the transmon in the dispersive limit (qubit detuned from resonator), in a frame rotating with the drive frequency. There is a photon term, a qubit term with a shifted frequency, and Rabi-flopping term from the resonator-qubit interaction. From this Hamiltonian, we will create our quantum gates.

Bit-flip

Simply by driving the system with $\Delta_a = -g^2/\Delta$, that is, *resonant with the shifted qubit frequency* $\omega_d = \omega_a + g^2/\Delta$, the σ_z term vanishes. The qubit will then rotate about the x-axis at the Rabi frequency, giving the X gate.

Phase-gate

Alternatively, if the drive is detuned from the (shifted) qubit frequency, that is, $\Delta_a + g^2/\Delta \gg \Omega_R$, then the drive should not induce qubit transitions, and we can adiabatically decouple the qubit from the drive (by the same procedure used to decouple the qubit from an off-resonant cavity). Applying the transformation $U = \exp[\frac{\Omega_R}{2\Delta_a}(\sigma^+ - \sigma^-)]$, we reduce the effect of the drive to just an energy shift [17]:

$$\mathcal{H} \approx \Delta_r a^\dagger a + \frac{1}{2}\left(\Delta_a + \frac{g^2}{\Delta} + \frac{\Omega_R^2}{2\Delta_a}\right)\sigma_z$$

So now the qubit frequency in the rotating frame has a shift from the detuned resonator and a shift from the detuned drive. The σ_x term has vanished, leaving only a phase rotation, which is controlled by the amplitude of the drive.

With the resonant x rotations and the detuned z rotations, we can perform any single-qubit gate [1].

4.3 Multi-qubit gates and entanglement

One major advantage of the transmission line is the natural structure for coupling qubits together. For instance, the transmission line length and frequency can be chosen such that multiple antinodes are present for coupling to qubits, as shown in Figure 4-2. This section will close the chapter with a brief mention of how such a system could be used to couple multiple qubits.

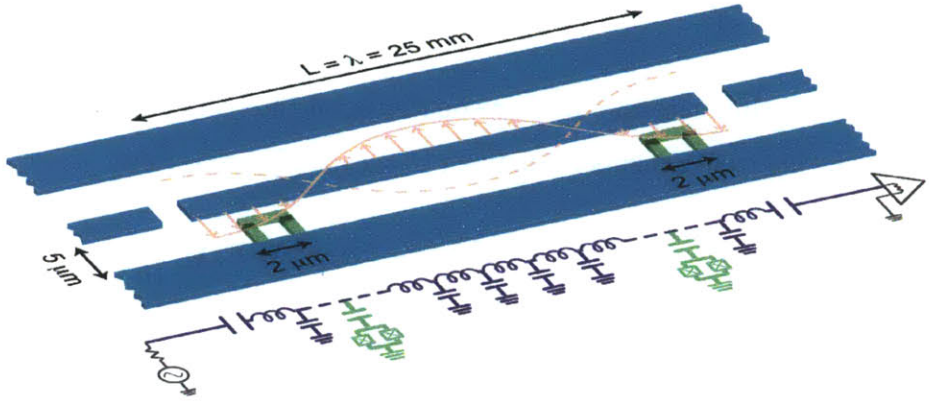

Figure 4-2: Multiple qubits can be strung along a single transmission line, far enough apart such that they only couple through a controllable resonator-based interaction. In this arrangement, each qubit has finite capacitance to the input or output gates of the resonator, which can be used to separately bias the individual qubit to its sweet spot. Reprinted from [17].

The Hamiltonian for this system [17] is the natural generalization of Eq 3.5:

$$\mathcal{H} = \hbar\omega_r \left(a^\dagger a + \frac{1}{2}\right) + \sum_{j=1,2} \frac{\hbar\Omega_j}{2}\sigma_{zj} - \sum_{j=1,2} \hbar g \left(a^\dagger \sigma_j^- + a\sigma_j^+\right) \tag{4.2}$$

where j indexes the qubits. This Hamiltonian provides two categories of approaches to couple the qubits to one another.

The first and most direct method is to tune Qubit 1 into resonance with the transmission line, let the Rabi-flopping encode Qubit 1's state upon the cavity photons, and then detune Qubit 1. Then choose the tuning of Qubit 2 in order to interact with the cavity photons as

desired, and, when finished, bring Qubit 1 back into resonance to transfer the photon state back into Qubit 1 and empty the cavity.

Exchanging information in such a manner through cavity photons requires that the cavity be of high quality so that information does not leak away during the gate. But experimenters often prefer to make use of lower quality cavities [5] so that the quality factor doesn't limit the speed of measurement pulses (measurement, as discussed, is performed near the cavity resonance). In this case, exciting photons in the cavity incurs losses to the environment, so one would prefer to remain in the dispersive regime with neither qubit directly coupled to the transmission line.

We can, as before, eliminate the direct resonator-qubit interaction to derive an effective Hamiltonian for the dispersive regime. Applying $U = \exp\left[\sum_j g_j/\Delta_j \left(a^\dagger \sigma_j^- - a\sigma_j^+\right)\right]$, we find

$$\mathcal{H} = \hbar\omega_r \left(a^\dagger a + \frac{1}{2}\right) + \sum_{j=1,2} \frac{\hbar}{2}\left(\Omega_j + \frac{g^2}{\Delta_j}\right)\sigma_{zj} + \frac{g_1 g_2(\Delta_1 + \Delta_2)}{2\Delta_1\Delta_2}\left(\sigma_1^+\sigma_2^- + \sigma_1^-\sigma_2^+\right)$$

The last term is a coupling between the two qubits which doesn't populate the cavity with photons. It can be interpreted as a second-order perturbative coupling via virtual photon exchange. By considering a rotating frame with either qubit frequency, it's straightforward to see that this interaction will only be strong if the qubits are tuned to the same frequency. (The same argument could be made by simple energy conservation.) The coupling by virtual photons thus provides a controllable method for coupling two qubits together, by tuning the qubits in or out of resonance with one another. This coupling generates what is known as the $\sqrt{\text{iSWAP}}$ gate in quantum information [17].

More complex methods for engineering the two-qubit interactions, which avoid having to tune the qubits, are too numerous to list here [17], but the above discussion should hopefully provide the basic ideas of how a transmon qubit is well-suited for multiple-qubit gates, a vital component for any non-trivial quantum computation. And with that, we have the basic ingredients for single and multiple qubit control and measurement.

Chapter 5

Summary

We have now discussed the Cooper Pair Box, the importance of the charging/inductive energy ratio, how to raise that ratio to convert the Cooper Pair Box into a transmon, how to couple the transmon with a resonator via the physics of Circuit QED, and how to use that coupling to perform operations on individual or multiple qubits. These are the basic ingredients to understanding a leading architecture for superconducting qubits.

The transmon has been modified in multiple ways since its original conception, for instance by replacing the transmission line with a fully three-dimensional waveguide cavity [26], but the basic concepts discussed herein remain central to understanding the system. The rapid growth of this architecture is exciting for the future of quantum computing. Perhaps the most convincing reason to follow the the transmon, or superconducting circuits in general is highlighted by the exponential trend of Figure 5-1.

This trend has been compared to Moore's law for classical computing [3]. Of course, workable single-qubit architectures are only the beginning. Forming these systems into full-scale quantum computers is still a daunting challenge, from which the world has much to gain, and scientists have much to learn. One practical way to simplify the early stages of scaling up from single-qubits is to make use of untouched higher levels in the system to increase the available computational space. The coming section will be devoted to mapping out these levels and determining their coherence properties.

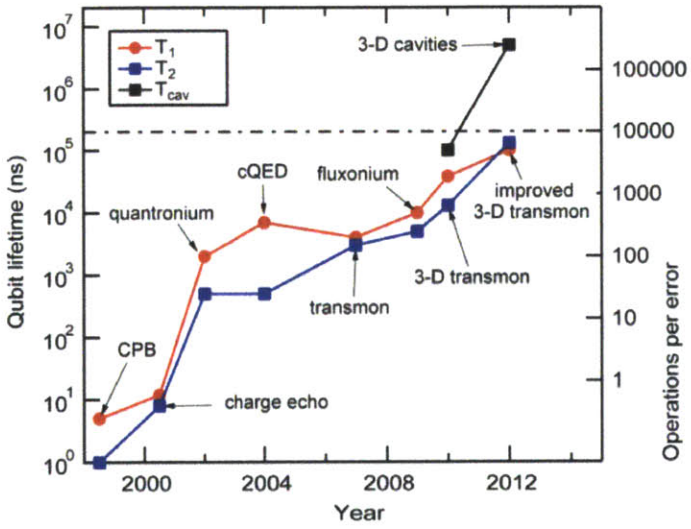

Figure 5-1: The timescale of qubit coherence in superconducting systems has seen exponential growth, from the early nanosecond-scale experiments with CPB systems, into the 100 µs-scale experiments with modern transmon variants. Reprinted from [3].

Part II

Experiment

Chapter 6

Setup

Now that the theory of the transmon has been laid out, and the well-developed literature using the two "computational states" has been reviewed, we will discuss the experimental methods for probing higher states for their potential use in computation.

6.1 Overall Scheme

As discussed in Section 4, the measurement of the qubit is obtained by measuring the transmission through the resonator. The overall heterodyne detection arrangement for performing these measurements upon a sample cooled to millikelvins in a dilution fridge is illustrated and explained in Figure 6-1.

The local oscillator (LO) is set to a frequency 50MHz above the RF generator. The two waves are mixed down together (1) before and (2) after passing through the sample, to produce a (1) reference wave and a (2) signal wave respectively. The phase of the signal wave can then be defined with respect to the reference wave.

All of the equipment is coordinated by a single trigger on repeat, and the signals are collected by an Acqiris digitizer. If the RF and LO generators have good phase stability (such that no significant phase drift between the two occurs during the averaging), then it is safe to average the signal traces together before fitting the amplitude and phase. This

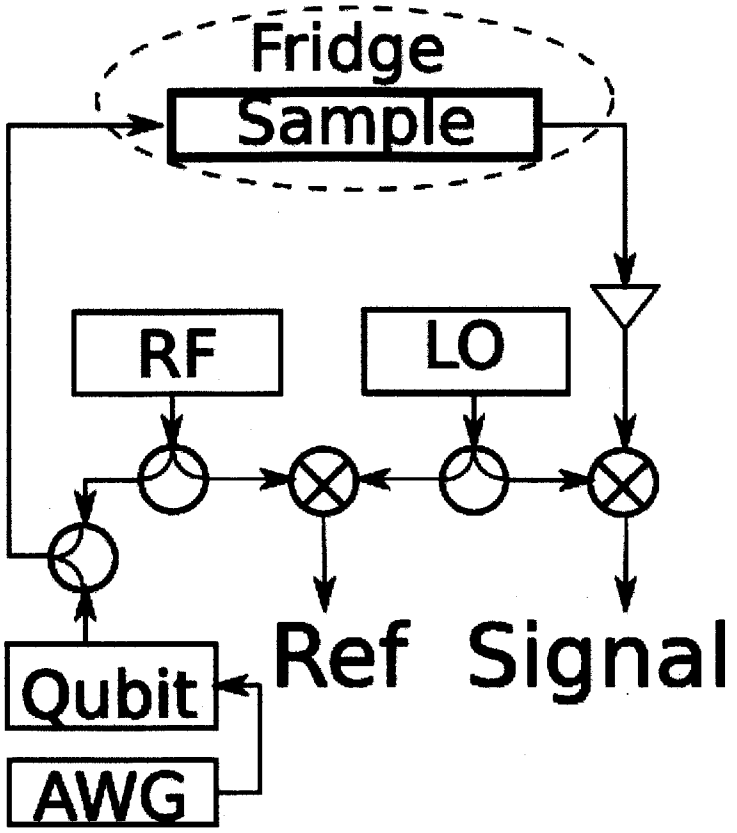

Figure 6-1: Heterodyne detection setup for measuring transmission through the sample. "RF", "LO", and "Qubit" are the Programmable Signal Generators (PSGs) for, respectively, pulsing at the resonator frequency, heterodyne comparison, and pulsing at the qubit frequencies. The Arbitrary Waveform Generator (AWG) connected to "Qubit" allows for more complex pulses described further on.

method is preferable in that the averaging can be done quickly in the hardware and the slow fitting step is used minimally.

However, equipment constraints at times forced us to rely on PSGs of lesser quality. In this case, phase drift on the timescale of the averaging results in mean cancellation of the signal traces. So it becomes necessary to fit individual signal traces to sinusoids and refer their complex amplitudes against the individual Reference traces *before* averaging. This is slower, but not intolerable. In practice, the phase drift is slow enough that some mix of the above two methods (eg averaging over a small number of traces before fitting, then repeating averaging/fitting many times) is often an acceptable speed-up.

6.2 Qubit Pulses and Single Sideband Mixing

The Qubit PSG and AWG combination is configured to use two channels "I" and "Q", which allows more detailed pulse control versus the on-off gated RF PSG. This configuration is illustrated in Figure 6-2. I is, by convention, the quadrature associated with pulses phased along the x-axis of the rotating frame Bloch sphere, and Q along the y-axis.

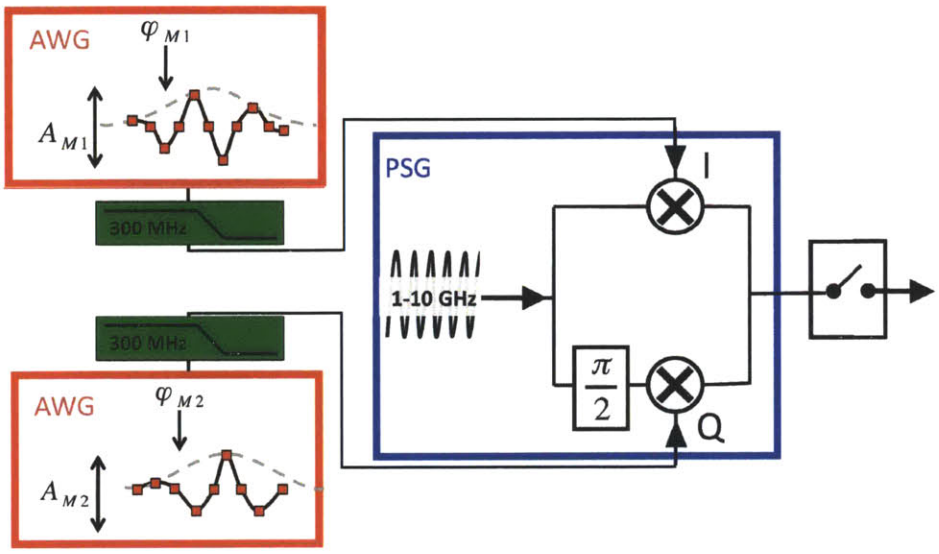

Figure 6-2: The I and Q ports of the PSG are connected to separate AWG outputs, and provide control over the two quadratures of the signal. The AWG can send simple on-off type pulses to control the I and Q channels, or may send sinusoidal modulations (as shown here) for more complex schemes. Image courtesy of Olger Zwier, modified.

Aside from simply using I and Q to control the phase of the qubit pulse (frequency f) about the Bloch sphere, the AWG can implement more complex schemes such as Single Sideband Mixing (SSBM). Modulating the AWG gate pulses by appropriately phased sinusoids at frequency f_m allows one to shift the output frequency to $f + f_m$. So the output frequency can be changed by adjusting the AWG waveform rather than the analog frequency source. One advantage to this scheme is that the PSG can be kept steady at a frequency far detuned from the qubit so that any leakthrough when the output is nominally gated off will not interfere with qubit dynamics.

Finally we implemented one more technique, known as DRAG (Derivative Removal via Adiabatic Gate), which is reshapes short pulse envelopes to reduce accidental driving of other transitions [27]. However, this feature of the setup has not been tested or benchmarked in our system yet, so we will not discuss it further.

Chapter 7

Procedure

7.1 Resonator

The first part to any experiment must be to determine the resonator frequency so that the qubit can be measured by resonator transmission. At low pulse power (where the resonator population is of the order of a few photons), the quantum effects discussed will dominate and the resonator frequency include a shift conditioned on the state of the qubit. At high enough power, the system behaves classically, and the transmission profile is centered about the "bare" cavity frequency.[1]

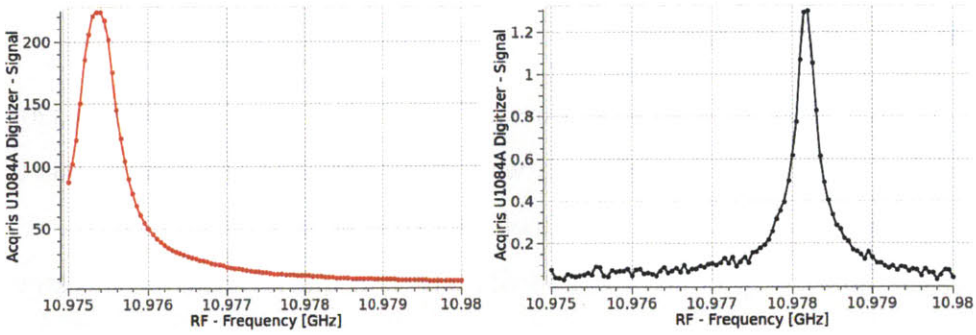

Figure 7-1: Resonator transmission profile in the high-power regime (left), showing the bare cavity frequency, and in the low-power regime (right), showing the cavity shifted by the qubit in State 0.

[1]Reviewing Eq. 3.2, our dispersive limit stops making sense for n on the order of $(\Omega/g)^2$.

7.2 Examining the 0-1 Transition

7.2.1 Spectroscopy

Once we have the resonator profile, we can sit our RF PSG on that State 0 peak, and apply pulses from the Qubit PSG to see if the transmission amplitude changes.

Applying a long drive pulse (longer than the coherence time of the qubit) at the 0-1 frequency, f_{01} will saturate the transition, so that the qubit is in a mixed state of being in State 0 half the time or State 1 half the time. So we would expect our RF transmission at the State 0 peak to fall to half its former value. Given this expectation, we can vary the drive frequency, and search for a dip in the transmission to find f_{01}.

Alternatively, applying a short drive pulse at the 0-1 frequency can drive the qubit into State 1, so we would expect our RF transmission at the State 0 peak to fall off to zero. Of course, since the drive flips the qubit between State 0 and State 1 periodically, one might just as easily drive, only to have the qubit end back in State 0 again, and the transmission would not change. In practice since the flipping frequency depends on the detuning, one generally finds, when scanning the drive frequency, a transmission dip modulated symmetrically by a sinusoid about the actual transition frequency.

7.2.2 Rabi and Ramsey

Rabi and Ramsey measurements are standard techniques in atomic physics [20], and the same principles apply in Cavity QED, so we will not dwell on the details, but it is worth pointing out how both fit into the scheme of the experiment.

Driving the qubit to produce Rabi oscillations is a quick means of checking that the drive frequency is actually resonant with a qubit, and by examining the oscillation, one can determine the correct amount of time to apply the drive so as to implement arbitrary angles of qubit rotation. This process is shown in Figure 7-2.

Once reasonable parameters for a $\pi/2$ pulse are known from Rabi measurements, it is easy to obtain the frequency (or *frequencies* in the case of charge dispersion) more precisely

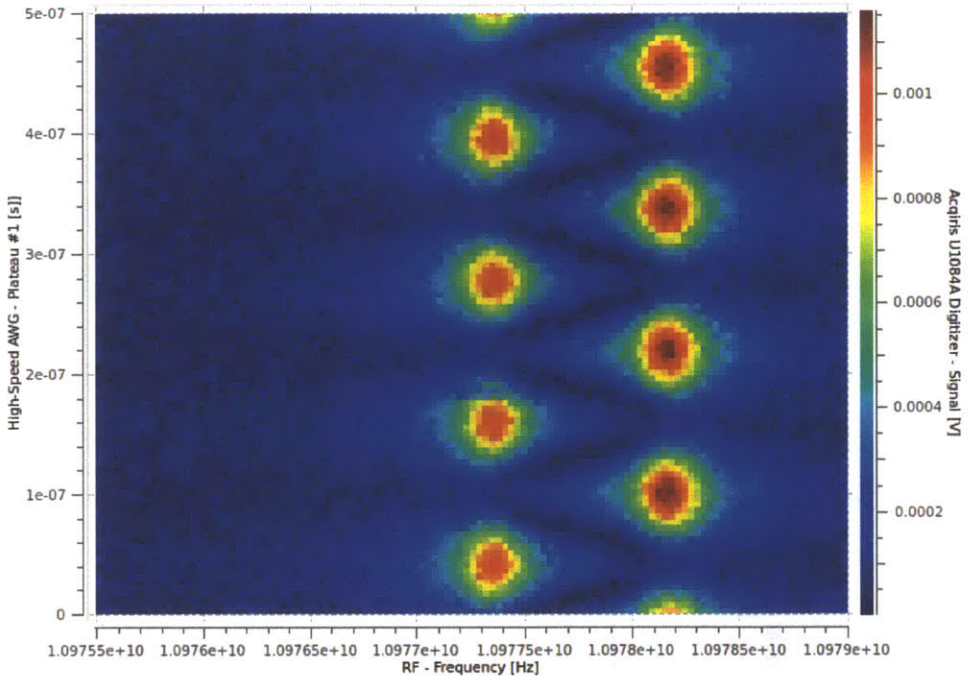

Figure 7-2: Rabi oscillations. The transmission profile (horizontal cross section) of the resonator vs duration of applied pulse (vertical axis) shows Rabi oscillations, switching between the profiles specific to State 0 (right) and State 1 (left). Note that the "pulse duration" does *not* include the rise/fall time, which is why the qubit is not in State 0 at "zero pulse duration."

from Ramsey measurements. One drives the qubit down to the x-axis with a $\pi/2$ pulse, allows a variable time to pass, and then applies a $\pi/2$ pulse again. If the pulses are perfectly resonant with the qubit, then the sum effect should bring the qubit to State 1.

However, if the drive is off in frequency, then a phase difference will accumulate between the qubit and the drive during the variable time, and the second pulse will not bring the qubit precisely to State 1. In fact, if a phase of π accumulates, the second pulse will bring the qubit to State 0! These oscillations of the final state occur at a frequency which is the difference between the qubit frequency and the drive frequency. So by applying a slightly detuned pulse, and measuring the oscillations versus waiting time, one can find out precisely how far off the detuned pulses are. This is shown in Figure 7-3.

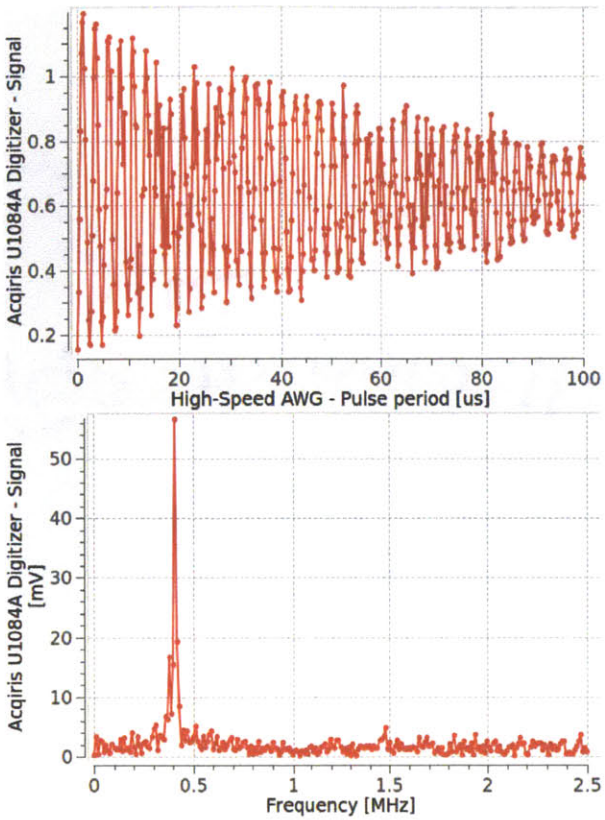

Figure 7-3: Ramsey oscillations (top) and their Fourier transform (bottom). The FFT spectrum shows one main resolvable peak for the transition (contrasted with say, Figure 7-5, where two frequencies are clearly visible for the 1-2 transition).

7.3 Examining higher transitions

In theory, one would expect the procedure for studying coherence in higher transmon levels to be the same as studying it in the 0-1 case. For instance, to study 1-2, do a π pulse to put the system into State 1, and then do Rabi and Ramsey measurements at the 1-2 frequency to your heart's desire. Readout can be done by sending in a pulse at the frequency which corresponds to the dispersive shift of State 1 (a frequency which can be read off of Figure 7-2).

In fact, this is the case for studying 1-2. But when we attempted the same measurements for 2-3, we ran into a difficulty; State 3 did not appear as a conditional shift to the resonator, and thus could not be read out. Figure 7-4 shows the results of an attempted

Rabi measurement between State 2 and State 3. The reason for this dismaying turn will be explained with the help of simulation results in Part 8.

But there is a work-around. The higher state transitions can actually be studied without doing the readout in higher states. For instance, if the experimenter wishes to know the population of State 2 after performing some experiment on the 2-3 transition, the experimenter can, instead of doing readout in State 2, apply pulses that would take State 2 to State 1 to State 0 and then do the readout in State 0. This method of indirect readout allows us to experiment on higher levels without ever performing troublesome readout of higher levels. As an example of this method, Ramsey oscillations on the 1-2 transition are shown in Figure 7-5.

One feature which becomes more prominent in the higher-level spectra is the splitting of transition frequencies. See, for instance, Figure 7-5. This can be explained by assuming that quasi-particle tunneling in the system switches the n_g of the transmon between two values, which, because of charge dispersion effects, leads to two different frequencies conditioned on the environment.

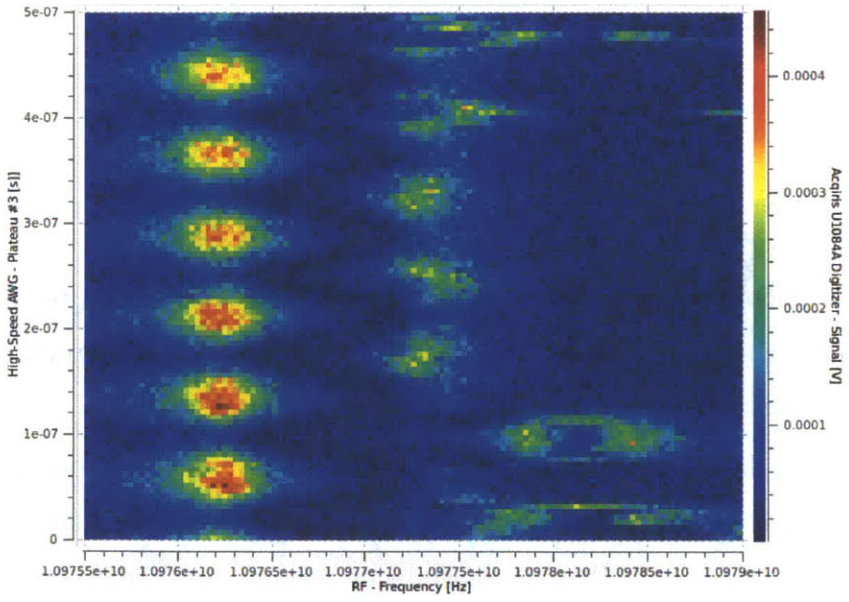

Figure 7-4: The Rabi measurement on 2-3 shows the appropriate resonator spectrum when the qubit is in State 2, but shows gibberish for State 3.

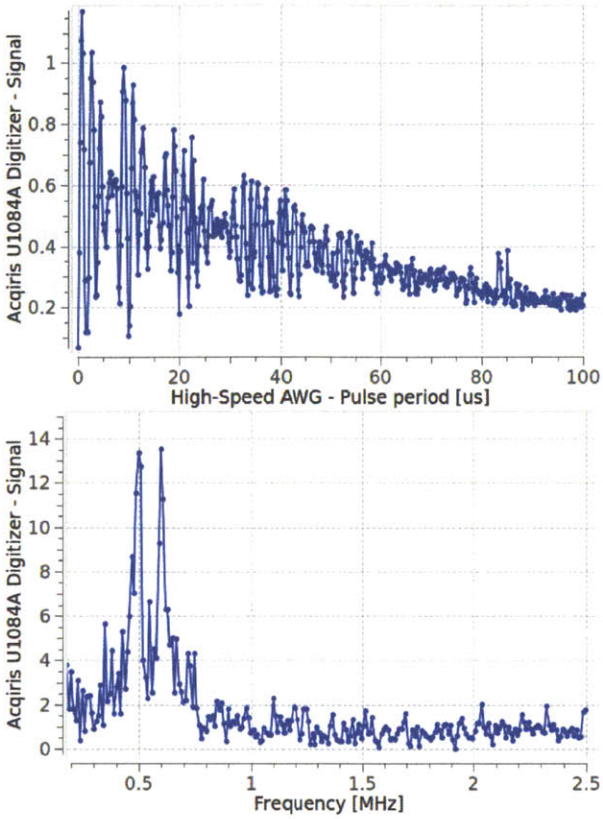

Figure 7-5: Ramsey oscillations (top) on the 1-2 transition and their Fourier transform (bottom). The two peaks in the FFT spectrum indicate that the qubit responds at two frequencies (separated by ~100 kHz).

7.4 Decays

Employing the readout scheme discussed in the previous section, it is possible to obtain decay traces showing the population of the various states versus time elapsed. The raw data to interpret is shown in Figure 7-6.

The calibration data (as shown in the figure) for any State n was obtained by simply pumping the population to state n and reading out State 0. So we see that State 0 provides a signal of about 2.3 mV to the State 0 transmission readout, and the other states provide a small (complex) contribution. The contribution of any other states is only non-zero due to the wings of the Lorentzian resonator transmission profile (and any decay to State 0 during readout). These transmission coefficients enable us to determine the actual state populations

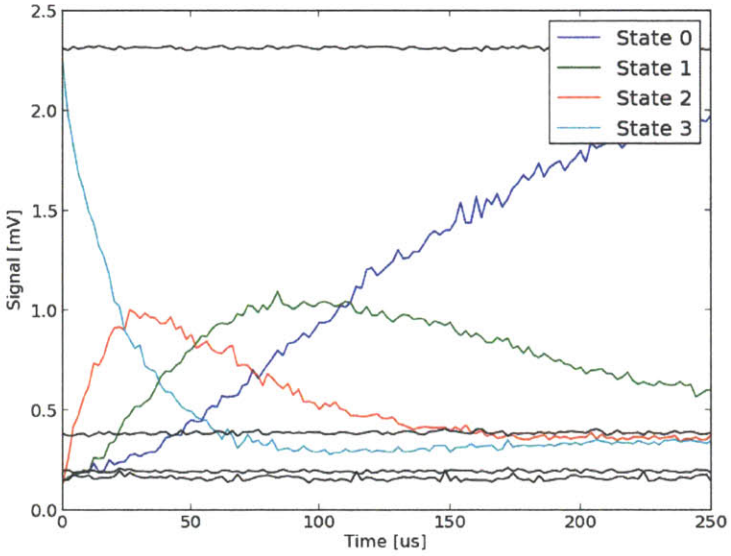

Figure 7-6: Signal traces for the population of each state (colored curves) during a decay from State 3, and calibration traces (black curves). The calibration curves give the (complex) contribution of each state (ordered 0 to 3 descending) to the readout transmission when fully populated, and can be used to convert the signal traces to populations.

from the results of an indirect readout on each level. This gives us dynamics as in Figure 7-7.

Those decay dynamics can then be fitted to determine the various transition rates between levels. The fitting can be done in several ways depending upon which conditions or physical assumptions one wishes to enforce. For example, the fitted 1-0 decay rate may vary unphysically between fits of the various decay traces. To avoid this nuisance, the traces are fitted in order of increasing complexity (ie clockwise from top-left in Figure 7-7), and any parameters fitted in one trace are held fixed in the next. So the first trace gives the 1-0 decay rate, then the second adds the 2-1 and 2-0, then the third adds the 3-2, 3-1, and 3-0 rates.

Further, one may want to restrict the various rates, since 2-0 and 3-1 are forbidden by parity arguments, and 3-0 should be so slow as to have no real effect on the decay. So these rates may be set to zero, as any value obtained for them is likely spurious. These assumptions

have all been lifted at various points to test the robustness of the fitting procedure, and the results do not change significantly.

The most prominent feature of the decay traces is that the decay proceeds sequentially (one transition at a time), and all other channels are strongly suppressed by two orders of magnitude. So it makes sense to describe the decays by a sequence of T_1 times. For States 1, 2, and 3, those are 84 μs, 40 μs, and 29 μs respectively, according to our fits.

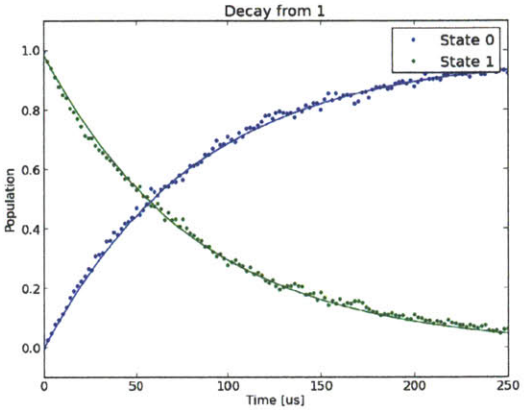

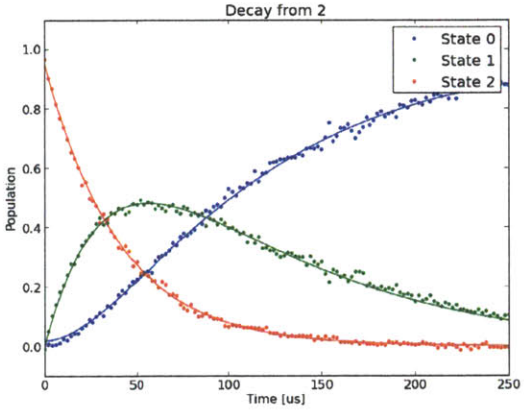

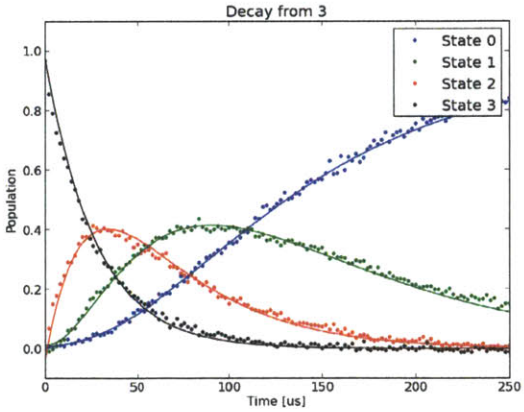

Figure 7-7: Populations during decays from States 1 through 3.

Chapter 8

Simulation

8.1 The Transmon

Computationally, the transmon qubit is a pleasure to work with. Either the energy spectrum and (phase-basis) wavefunctions can be given exactly in terms of Mathieu functions as discussed in Section 2.1.2, or the Hamiltonian can be solved in the charge basis using Eq. 2.1. For full generality, and to encourage a smooth transition into simulation of the coupled system, we will use the latter approach here: starting in the charge basis and diagonalizing the Hamiltonian. This section will walk through the details of the simulation, and, unless otherwise mentioned, examples and figures given here use the qubit parameters fitted from our experiment, a procedure which will be discussed later.

As noted, the transmon Hamiltonian contains two parts: a charging term, and a Josephson term. Working in the charge basis, the first term is already diagonal, and thus easy to represent. The second term also allows a convenient writing in terms of the charge variable. And even if it did not, we could still, in generality, easily and efficiently find its matrix elements in the charge basis: the second-term is naturally given in the phase, which can be taken to the charge by a Fast Fourier Transform (since charge eigenfunctions are plane waves in the phase basis).

To solve the system numerically, we must, of course, restrict our calculation to a finite

basis. Hopefully, the important (low) energy levels can be properly captured by linear combinations of some relatively small set of charge basis functions. In practice, this is the case, and the "effective completeness" of our restricted basis is the very first simulation aspect that should be checked to avoid introducing artifacts into later results. As we see in Figure 8-1, the states we care about have negligible projections onto all charge states beyond about $|n| = 10$. The wavefunctions and energy levels are given in Figures 8-2 and 8-3.

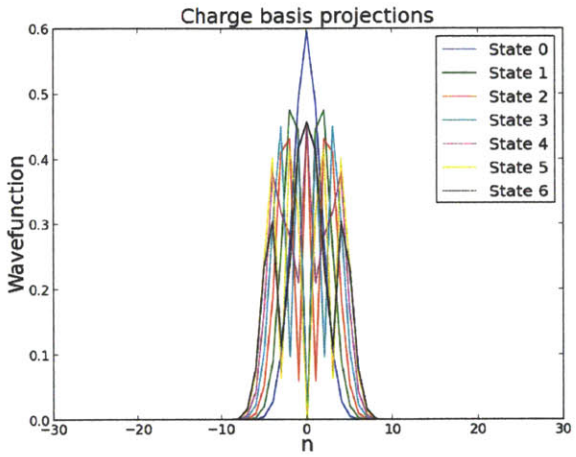

Figure 8-1: Checking the completeness of the restricted charge basis.

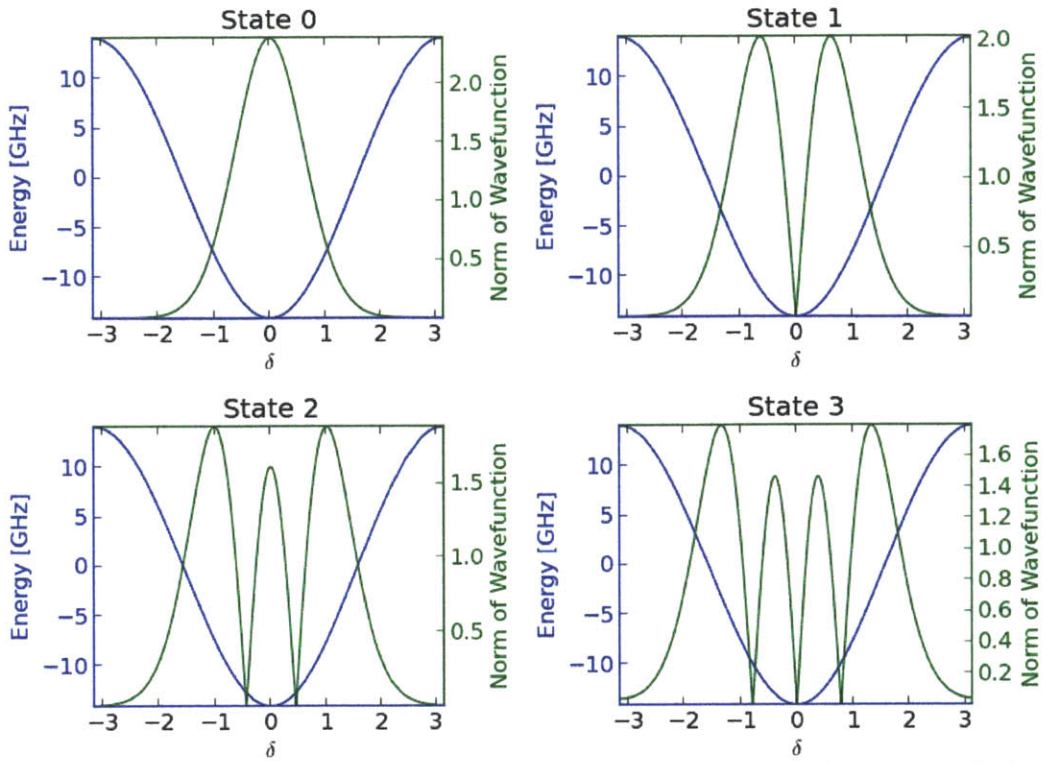

Figure 8-2: Wavefunctions for the lowest four levels, visually similar to simple harmonic oscillator wavefunctions. Note that the lack of Gibbs phenomena (extraneous oscillations) provides another check on the completeness of our basis.

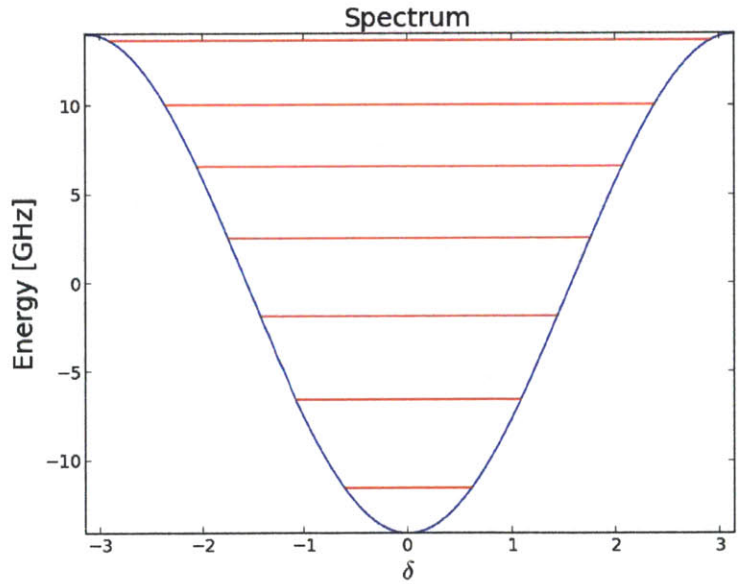

Figure 8-3: Simulated spectrum

8.2 The Coupled System

Now we take our verified transmon simulation and couple it into a resonator, where the Hamiltonian for the total system is given by Eq. 3.4. Certainly, we could have simply started with the full Hamiltonian and diagonalized it all at once, but there is an advantage to diagonalizing the transmon beforehand as we have done. Notice that the dimension of the total system is the product of the number of transmon restricted basis states with the number of resonator restricted basis states. If we have already solved the transmon, we can simply take the transmon levels of interest, rather than all of the charge basis states necessary to construct it. This makes the total system re-diagonalization faster since the matrices involved are smaller.

The resonator is described by a simple harmonic oscillator, so its raising and lowering operators have the well-known matrix elements. And since the transmon has been diagonalized, we have the matrices for its Hamiltonian and for the charge operator which couples to the resonator. By taking the Kronecker products of these various subsystem matrices with subsystem identity matrices, we obtain matrices which act appropriately upon the total system. We then diagonalize the total Hamiltonian, and, effortlessly, have our new spectrum. The nontrivial part is how we analyze this numerical spectrum to obtain the intuitive descriptive properties of the resonant and dispersive limits discussed in Section 3.1.2.

To recap, if two transmon levels are in the dispersive regime (their transition is far-detuned from the cavity), then the transmon state and the resonator state are nearly good quantum numbers, and the main effect of the coupling is just to shift the energies. So it makes intuitive sense, in Figure 3-2(b), to draw the spectrum as multiple columns identified by a qubit state. On the other hand, if the transition is resonant with the cavity, then the transmon levels mix and it makes intuitive sense, in Figure 3-2(a), to draw the coupled spectrum in between the unperturbed columns. We will now try to generalize this convention to the many-level transmon by defining the *mean transmon value.*

This mean transmon value is a property of any energy eigenstate of the total system. If we write the eigenstate in terms of the unperturbed basis states (the states with well-

defined transmon levels and resonator occupations), the eigenstate will generically include projections onto many different unperturbed states of the transmon (which we call "State 0", "State 1",... etc). If we treat the state names (0,1, etc) as numerical values, we can take the projection-weighted "mean" transmon state for any eigenstate. Since the state names do not have any meaning (other than ordering the eigenvalues), their mean is obviously not a "physical" quantity, but it is well-defined and useful for intuitive descriptions of the spectrum, as follows.

If two transmon levels (say State 1 and State 2) are in the dispersive regime, we expect to find in our spectrum a tower of equally spaced total eigenstates with mean transmon value close to 1, distinguished by different resonator occupations, and a similar tower with mean transmon value close to 2, shifted up in energy by the 1-2 transition frequency. That is, clustering the spectrum by the mean transmon value produces a plot like 3-2(b). Alternatively, if two levels (say State 1 and State 2) are in the resonant regime together, we expect to find in our spectrum a set of paired states with mean transmon value close to 1.5, ie the middle of 3-2(a). If two levels (say State 1 and State 2) are in some intermediate regime, we expect relatively separated states at low resonator occupations (some close to 1, some close to 2), which merge toward 1.5 at higher resonator occupations.

Essentially, the looking at the mean transmon value for a total eigenstate can tell us whether it is being pulled away from its unperturbed composition by some coupling. Note that this is not a perfect metric in isolation. For instance, if State 1 and State 3 are resonantly coupled, then there might be dressed total eigenstates composed of State 1 and State 3, with mean transmon value close to 2. But this is not part of the State 2 spectrum, it is a mix of State 1 and State 3. But in practice, viewing a plot, this is not difficult to pick out, and one can always check to see what the actual composition of a total eigenstate is. The intention of introducing this unphysical parameter is to produce plots like Figure 8-4.

The features of Figure 8-4 will be important in analyzing our experimental results in Part II. First, let us just consider the spectra of the"well-behaved dispersive states" in the first three columns. These states can be neatly grouped by their mean transmon value, and each

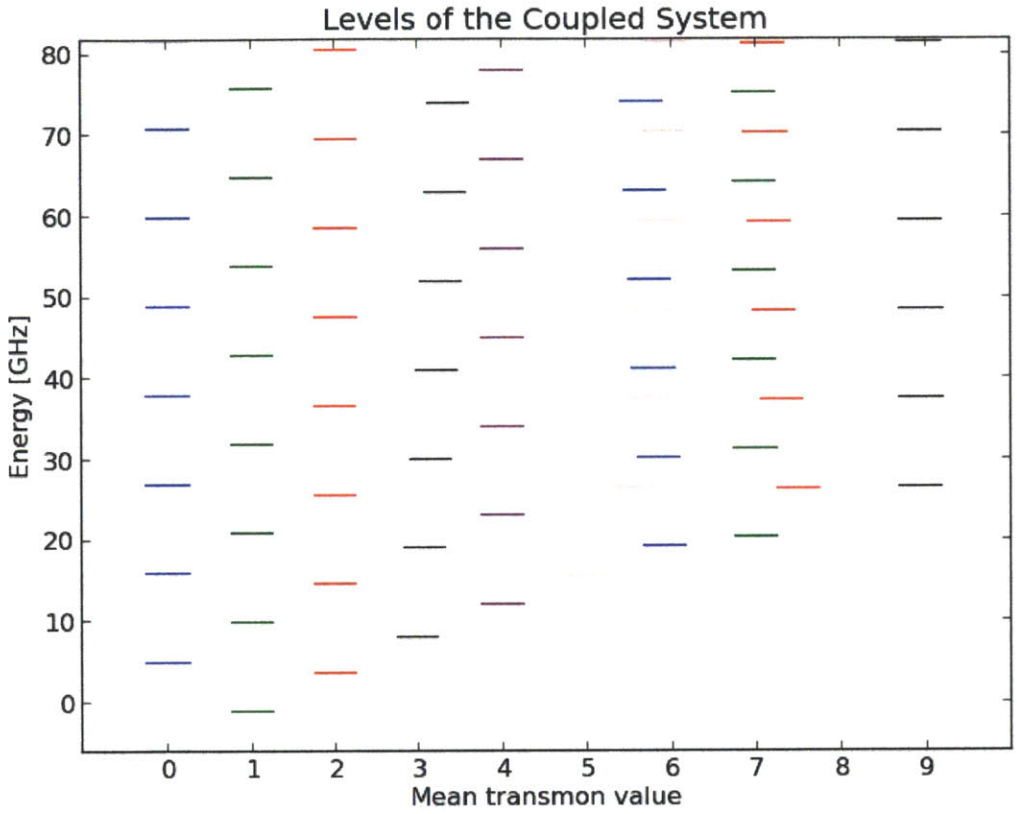

Figure 8-4: The total system spectrum, plotted versus the intuitive "mean transmon value." This type of plot keeps dispersively coupled levels neatly organized by their approximately good transmon quantum number, but makes resonantly coupled levels lean in toward each other. Here, states 3 and 6 mix together, as well as 5 and 8.

forms its own simple harmonic oscillator spectrum. So we can programmatically extract meaningful physical quantities once the spectra are clustered.

The frequency difference between pairs of levels in the State 0 cluster gives us the resonator frequency conditioned on the qubit being in State 0, and likewise for the State 1 cluster. So we have all the dispersive shifts laid out for us. And the frequency difference between the lowest State 0 level and the lowest State 1 level is the effective transition frequency between those two transmon states as modified by the resonator coupling. Once the eigenstates are clustered, we have all of the intuitive properties to describe our system.

And, for the levels we cannot cluster neatly, these properties simply do not make sense anyhow. For example, Figure 8-4 shows various "leaning towers", and analysis of the components of the eigenstates confirms that levels 3 and 6 are mixing, and levels 5 and 8 are mixing. Consequently, it does not make much sense to discuss a conditional dispersive shift for State 3, since the spacing of the states in the State 3 leaning tower is not very uniform (ie the tower has significant non-anharmonicity). The fact that this appears in State 3 for our simulation explains the difficulty that we had in reading out State 3 experimentally via its dispersive shift.

While we are modeling the properties of the system, we can also capture charge dispersion effects, since n_g is now an explicit parameter under our control. As discussed in Section 2.2.1, we expect the 0-1 transition in a transmon to be stable with respect to charge fluctuations. Now we can look at the dispersion for other levels as well, as in Figure 8-5. All of these properties will be summarized for reference in Chapter 9.

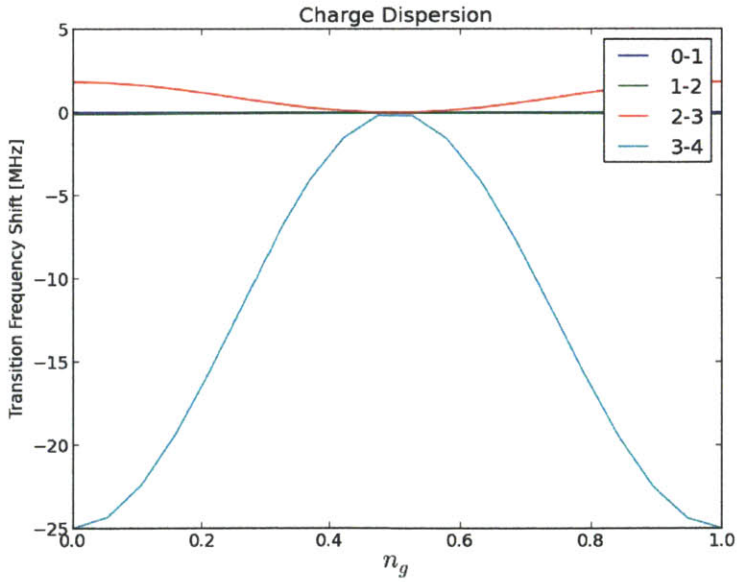

Figure 8-5: How the transition frequencies vary with charge fluctuations. We see that the dependence becomes larger for higher levels which are not as deep in the potential well.

Chapter 9

Results

9.1 Fitting

There are four parameters available to the simulation: the E_J and E_C of the qubit itself, the bare frequency f_r of the resonator, and the coupling g_{01} between the resonator and the qubit.[1]

The value of f_r we can easily extract from probing the resonator at high power as discussed in Part II. E_J and E_C we vary in order to fit the first two qubit transition frequencies. And g_{01} we vary to fit the dispersive shift of State 0. Once those parameters are chosen, the model is entirely fixed, so its predictions of the higher transition frequencies and other dispersive shifts are valuable indicators of the accuracy of our simulation.

9.2 Values

Tables 9.2 and 9.1 show the various values measured on our transmon and predicted by our simulation. The model was fit to the first two frequencies and the State 0 dispersive shift; these fixed values are starred in the tables. The model then predicts the next two transition

[1]Note that before, in Part I, we used g with no subscript to couple the resonator and qubit, but now the subscript is present to indicate that this is the coupling strength specific to the 0-1 transition. The other coupling strengths are not free parameters once g_{01} is fixed, but rather are related to g_{01} by the ratios of the charge matrix elements between transmon levels.

frequencies and the next two dispersive shifts to within the experimental frequency splitting (charge dispersion). It also captures the rough scaling of the splittings. The parameter values obtained from the fits are shown for reference in Table 9.3.

Transition	0-1	1-2	2-3	3-4
Experimental frequency	4.9692 GHz	4.6944 GHz	4.3855 GHz	4.0280 GHz
Model frequency	*4.9692 GHz	*4.6944 GHz	4.3874 GHz	4.0475 GHz
Experimental Splitting	< 30 kHz	100 kHz	2.5 MHz	5-10? MHz
Model charge dispersion	2.5 kHz	88 kHz	1.8 MHz	25 MHz

Table 9.1: Frequencies measured and predicted, and measured frequency splittings in comparison with predicted charge dispersion. The bound on the experimental 0-1 splitting comes from the fact that it is unresolved.

State	0	1	2	3
Experimental shift	2.8	2.0	.88	invalid
Model shift	*2.8	2.0	.85	invalid

Table 9.2: Dispersive shifts [MHz] as measured and predicted. The experimental shift for State 3 is listed as invalid as shown in Figure 7-4, and the model appropriately produces an ill-defined shift for this state, as shown in Figure 8-4.

System parameter	f_r	E_J	E_C	g
Fitted Value	10.97537 GHz	14.07064 GHz	243.12372 MHz	1644.84738 MHz

Table 9.3: Fitted values for the system, used in defining the Hamiltonian to extract all of the above simulation results.

Also, although we do not have the noise spectrum in the resonator, which would be necessary in order to produce realistic decay rates from our simulation results, we can show how the decay rates would scale with various assumptions about the noise, as in Table 9.4. The simulation data gives charge matrix elements, which are connected to the decay rates by Fermi's golden rule[2]. Without knowing the noise explicitly, we can at least scale up the matrix element to match the decay rate for the 0-1 transition, and using that scale factor, guess what the decay rates for the other transitions should be.

[2]Note that the detuning does not explicitly enter here because we are not in a Purcell-limited regime

Transition	0-1	1-2	2-3
Experimental rate	84	40	29
White noise	*84	45	32
$1/f$ noise	*84	42	28

Table 9.4: Decay rates experimental and predicted for all transitions under various noise assumptions

9.3 Conclusion

The simulation successfully captured the frequencies and dispersive shift of the transmon, as well as the rough scaling of the frequency splittings due to charge dispersion. Most importantly, it was able to explain the strange phenomena associated with State 3 due to its accidental coupling with State 6.

The model also predicts that any non-sequential transitions will be strongly suppressed, which fits with the decay data; without further study of the noise spectrum in the system, we cannot yet say much numerically regarding the predicted decay rates, but we do have at least this qualitative agreement. And the simulation, with reasonable assumptions about the resonator noise, does capture the trend of decay rates.

So, in summary, we have examined the basic coherence properties of the higher levels of a transmon system for the possibility of extending computational schemes beyond the qubit, and we have found them to fit the predictions of our model. This is an exciting avenue of research which opens up the possibility of furthering quantum computation which algorithms that take advantage of the expanded state-space already present in transmon qubits.

Part III

Appendix

Appendix A

Derivation of Classical Hamiltonians for Qubit Systems

These derivations follow a standard procedure [28] for the writing the Hamiltonians of classical circuits.

A.1 Cooper Pair Box

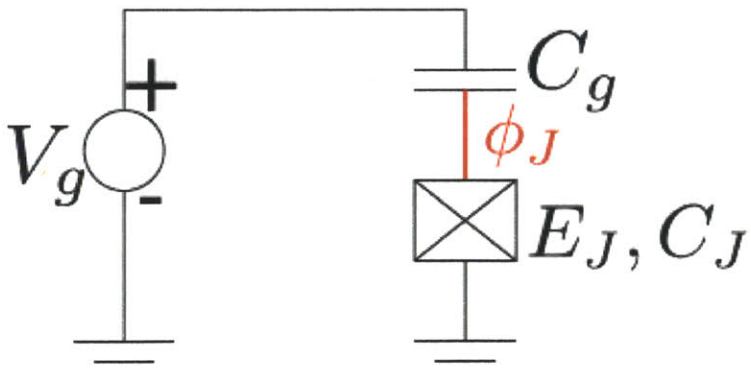

Figure A-1: Circuit for the Cooper Pair Box, with the node flux variable marked.

The Cooper Pair Box circuit is straightforward to model. Once we remove the voltage source, there is only one node other than ground, as shown in Figure A-1. Our kinetic part

will include a charging term for both capacitances:

$$T = \frac{C_g}{2}\dot{\phi}_J^2 + \frac{C_j}{2}\dot{\phi}_J^2 = \frac{C_\Sigma}{2}\dot{\phi}_J^2$$

where $C_\Sigma = C_g + C_j$ is the total island capacitance. Our potential terms will include the Josephson term and the external source energy. The energy which the source supplies is V_g times charge on the supply-side of the gate capacitor. This charge can be written as the voltage across the gate capacitor ($-\dot{\phi}_J$) times the gate capacitance C_g. Putting that together,

$$U = -E_j \cos\left(\frac{2\pi}{\Phi_0}\phi_J\right) - V_g C_g \dot{\phi}_J$$

The Lagrangian is then

$$\mathcal{L} = T - U = \frac{C_\Sigma}{2}\dot{\phi}_J^2 + E_j \cos\left(\frac{2\pi}{\Phi_0}\phi_J\right) + V_g C_g \dot{\phi}_J$$

The conjugate momentum is the charge in the island plus an effective offset charge gated by the source.

$$Q_J = \frac{\partial \mathcal{L}}{\partial \dot{\phi}_J} = C_\Sigma \dot{\phi}_J + V_g C_g$$

The Hamiltonian is then

$$\mathcal{H} = Q_J \dot{\phi}_J - \mathcal{L} = \frac{(Q_J - C_g V_g)^2}{2C_\Sigma} - E_J \cos\left(\frac{2\pi}{\Phi_0}\phi_J\right)$$

It is often written in terms of δ, the gauge invariant phase across the junction,

$$\mathcal{H} = Q_J \dot{\phi}_J - \mathcal{L} = \frac{(Q_J - C_g V_g)^2}{2C_\Sigma} - E_J \cos(\delta)$$

A.2 Transmon with transmission line

The transmon is only slightly more complicated, requiring two node flux variables. For convenience, we will simply lump the Josephson capacitance C_J into the shunt capacitance

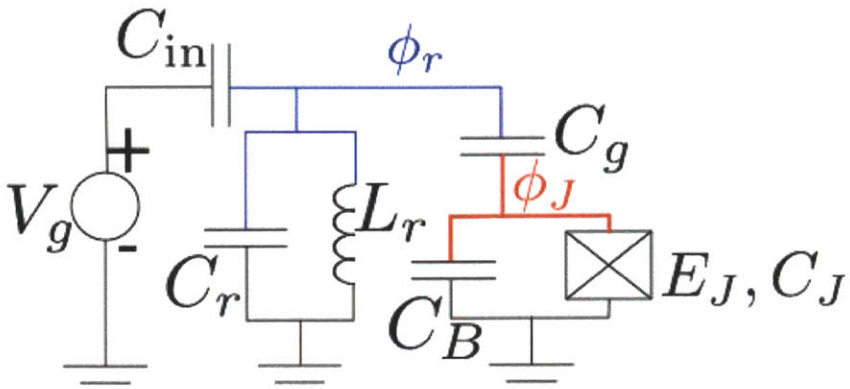

Figure A-2: Effective circuit for the Transmon, with two node flux variables.

C_B. The kinetic terms are the charging terms for each capacitor:

$$T = \frac{C_{\text{in}}}{2}\dot{\phi}_r^2 + \frac{C_r}{2}\dot{\phi}_r^2 + \frac{C_g}{2}\left(\dot{\phi}_J - \dot{\phi}_r\right)^2 + \frac{C_B}{2}\dot{\phi}_J^2$$

The potential terms include the resonator effective inductance, the Josephson term, and the external energy source, written as before:

$$U = \frac{1}{2L}\phi_r^2 - E_j \cos\left(\frac{2\pi}{\Phi_0}\phi_J\right) - V_g C_{\text{in}}\dot{\phi}_r$$

The Lagrangian is then

$$\mathcal{L} = \frac{C_{\text{in}}}{2}\dot{\phi}_r^2 + \frac{C_r}{2}\dot{\phi}_r^2 + \frac{C_g}{2}\left(\dot{\phi}_J - \dot{\phi}_r\right)^2 + \frac{C_B}{2}\dot{\phi}_J^2 - \frac{1}{2L}\phi_r^2 + E_j \cos\left(\frac{2\pi}{\Phi_0}\phi_J\right) + V_g C_{\text{in}}\dot{\phi}_r$$

The conjugate momenta are more complicated:

$$Q_r = \frac{\partial \mathcal{L}}{\partial \dot{\phi}_r} = (C_{\text{in}} + C_r + C_g)\dot{\phi}_r - C_g\dot{\phi}_J + V_g C_{\text{in}}$$
$$Q_J = \frac{\partial \mathcal{L}}{\partial \dot{\phi}_r} = (C_J + C_g)\dot{\phi}_J - C_g\dot{\phi}_r$$

And the Hamiltonian, after a great deal of algebra, becomes, up to a constant

$$\mathcal{H} = Q_J\dot{\phi}_J + Q_r\dot{\phi}_r - \mathcal{L}$$

$$
\begin{aligned}
= & \frac{\phi_r^2}{2L_r} + \frac{(C_B + C_g)\, Q_r^2}{2C_*^2} \\
& + \frac{(C_g + C_{\text{in}} + C_r)\, Q_J^2}{2C_*^2} - E_J \cos\left(\frac{2\pi}{\hbar}\phi_J\right) \\
& + \frac{C_g Q_r Q_j}{C_*^2} + \frac{(C_b C_{\text{in}} + C_g C_{\text{in}})\, Q_r V_g + C_g C_{\text{in}} Q_J V_g}{C_*^2}
\end{aligned}
$$

where

$$
C_*^2 = C_B C_g + C_B C_{\text{in}} + C_g C_{\text{in}} + C_B C_r + C_g C_r
$$

in agreement with [4]. The first line is the resonator term, the second is the qubit, and the third is all of the intercouplings. In the reasonable limit that C_r is much greater than all other capacitances, this reduces to

$$
\begin{aligned}
\mathcal{H} = & \frac{\phi_r^2}{2L_r} + \frac{Q_r^2}{2C_r} \\
& + \frac{Q_J^2}{2C_\Sigma} - E_J \cos\left(\frac{2\pi}{\hbar}\phi_J\right) \\
& + \beta \frac{Q_r Q_j}{C_r} + \frac{C_{\text{in}} Q_r V_g}{C_r}
\end{aligned}
$$

where $C_\Sigma = C_g + C_B$ and $\beta = C_g/C_\Sigma$ is an impedance divider ratio which determines how much of the transmission line voltage is seen by the qubit.

The last term of the above expression does not disappear in the limit of large C_r, because Q_r is also large (such that their ratio is the voltage on the resonator). However, the term coupling Q_J and V_g *did* vanish. Naively, this is worrisome because that was the term which we would have expected to provide an effective offset charge (as in the CPB case) which allows use to tune the qubit energy levels.

This trouble appears because our lumped LC model of the resonator is only valid for wavelengths on the scale of the resonator [17]; it does not work at DC.[1] In actuality, the resonator is just a capacitor at DC, and (again assuming C_r to be the largest capacitance in the system), any DC gate voltage will show up at the gate capacitor, and have the same

[1]Applying the LC model at DC would for would force the centerline of the resonator to always have zero DC voltage, because otherwise the current through the "effective inductor" increases to infinity.

effect it would have in the CPB system. We can add this DC term in to produce the final form of the classical Hamiltonian.

$$\begin{aligned}\mathcal{H} = & \frac{\phi_r^2}{2L_r} + \frac{Q_r^2}{2C_r} \\ & + \frac{\left(Q_J - C_g V_g^{\mathrm{DC}}\right)^2}{2C_\Sigma} - E_J \cos\left(\frac{2\pi}{\hbar}\phi_J\right) \\ & + \beta\frac{Q_r Q_j}{C_r} + \frac{C_{\mathrm{in}} Q_r V_g}{C_r}\end{aligned}$$

Appendix B

Quantum Circuits

Superconducting electrical circuits can be quantized [28] by imposing a canonical commutation relation between flux variables and charge variables, $[\hat{\Phi}, \hat{Q}] = i\hbar$. Since our circuits will prominently feature Josephson junctions, we will conveniently consider this relation in terms of superconducting phase difference $\hat{\delta}$ across an element and its conjugate momentum, a population difference $\hat{N}$ of Cooper pairs across an element. In terms of these unitless variables the relation becomes $[\hat{\delta}, \hat{N}] = i$.

B.1 Charge basis

For circuits where the energy is mainly capacitive, we will find it useful to work with a basis of charge eigenstates $\{|n\rangle\}$, with $\hat{N}|n\rangle = n|n\rangle$. For concreteness, imagine the Cooper pair box, that is, a superconducting island connected to charge reservoir by a Josephson junction, wherein $|n\rangle$ represents the state in which n Cooper pairs have tunnelled into the island.

First we show that $e^{\pm i\hat{\delta}}$ are raising and lowering operators for charge [29].

$$\begin{aligned}\left[\hat{N}, e^{\pm i\hat{\delta}}\right] &= \left[\hat{N}, \sum_{\alpha=0}^{\infty} \frac{(\pm i\hat{\delta})^{\alpha}}{\alpha!}\right] \\ &= \sum_{\alpha=0}^{\infty} (\pm i)^{\alpha} \frac{[\hat{N}, \hat{\delta}^{\alpha}]}{\alpha!}\end{aligned}$$

$$
\begin{aligned}
&= \sum_{\alpha=0}^{\infty} (\pm i)^{\alpha} \frac{-\alpha i \hat{\delta}^{\alpha-1}}{\alpha!} \\
&= \pm \sum_{\alpha=1}^{\infty} i^{\alpha-1} \frac{(\pm\hat{\delta})^{\alpha-1}}{(\alpha-1)!} \\
&= \pm \sum_{\alpha=0}^{\infty} i^{\alpha} \frac{(\pm\hat{\delta})^{\alpha}}{(\alpha)!} \\
&= \pm e^{\pm i\hat{\delta}}
\end{aligned}
$$

Since $e^{i\hat{\delta}}$ is manifestly unitary, we can choose phases such that $e^{\pm i\hat{\delta}} |n\rangle = |n \pm 1\rangle$, that is

$$
e^{\pm i\delta} = \sum_{n} |n \pm 1\rangle \langle n|
$$

Since the Hamiltonian generally contains a Josephson term proportional to the cosine of the phase, we will often find it useful to write [15], [29]

$$
\cos\hat{\delta} = \frac{1}{2}\left(e^{i\hat{\delta}} + e^{-i\hat{\delta}}\right) = \frac{1}{2}\left(\sum_{n} |n+1\rangle \langle n| + |n-1\rangle \langle n|\right) \tag{B.1}
$$

B.2 Phase basis

Alternatively, we could work with wavefunctions $\psi(\delta)$ in δ-space. In this representation, we can satisfy the commutation relation $[\hat{\delta}, \hat{N}] = i$ the same way it is done in the Schrödinger equation: by choosing [15]

$$
\hat{\delta} = \delta, \qquad \hat{N} = -i\frac{\partial}{\partial\delta}
$$

This representation has the convenience of being continuous, so that one may view the equations of motion of a superconducting circuit within an analogy to the quantum mechanics of a one-dimensional particle. For instance, in the Cooper-pair box Hamiltonian discussed in Section 2.1:

$$
H = 4E_C\left(-i\frac{\partial}{\partial\delta} - n_g\right)^2 - E_J\cos\delta
$$

the equations of motion would be identical to that of a 1-D particle in a cosine potential, as discussed in C.1.

Appendix C

Perturbation Theory for the Transmon

Although the spectrum for the transmon can be given in terms of Mathieu functions as mentioned in Sec 2.1.2, it will be useful to have some simple expressions for the energies when evaluating properties of the transmon in the large E_J/E_C limit.

C.1 Periodic Potentials

However, before we undertake this task, it will be beneficial to consider more closely the connection made between the CPB Hamiltonian and the particle in a periodic potential, because a subtlety will arise in the handling of the offset charge n_g which can be explained clearly in this analogy. This familiar Hamiltonian is

$$\mathcal{H}_{\text{crystal}} = \frac{-\hbar^2}{2m}\frac{\partial^2}{\partial x^2} + V(x), \quad \text{with } V(x+a) = V(x)$$

By the periodicity, Bloch's Theorem states that the eigenstates can be written in the form

$$\psi_{kn}(x) = e^{ikx}u_{kn}(x)$$

for some $u_{kn}(x)$ such that $u_{kn}(x+a) = u_{kn}(x)$. Plugging in this form and pulling the exponential through the derivatives, the Schrodinger equation can be rewritten

$$E_{kn}u_{kn}(x) = \left[\frac{\hbar^2}{2m}\left(-i\frac{\partial}{\partial x} + k\right)^2 + V(x)\right] u_{kn}(x)$$

with the boundary condition that $u(0) = u(a)$, $u'(0) = u'(a)$. It is vital to note that the u_{kn} are exactly periodic, not "periodic up to a phase" like the full Bloch eigenstates ψ_{kn}. So we have an effective Hamiltonian $\mathcal{H}_{\text{eff},k}$ for the k wavevector states $u_{kn}(x)$:

$$\mathcal{H}_{\text{eff},k} = \frac{\hbar^2}{2m}\left(-i\frac{\partial}{\partial x} + k\right)^2 + V(x) \tag{C.1}$$

which is the same form as the CPB Hamiltonian:

$$\mathcal{H}_{\text{CPB}} = 4E_C\left(-i\frac{\partial}{\partial \delta} - n_g\right)^2 - E_J\cos\delta \tag{C.2}$$

And the CPB problem carries the same boundary condition as the u_{kn}: the wavefunction must be periodic, $\psi(-\pi) = \psi(\pi)$, $\psi'(-\pi) = \psi'(\pi)$. (This follows from insisting that the eigenvalues of $N = -i\frac{\partial}{\partial\delta}$ must be integers, so the solution space is spanned by a basis $e^{in\delta}$ which repeats every 2π.)

The mapping between these two problems is the similarity between Eq C.1 and C.2.

C.2 Transforming away the offset charge

Naively, one might think that the offset charge could be removed from the CPB Hamiltonian by writing

$$\psi_{n_g a}(\delta) = e^{-in_g\delta}u_{n_g a}(\delta)$$

essentially doing the inverse of the Bloch's theorem step above to acheive an offset-free effective Hamiltonian. The reason that this trick doesn't help in general is that it merely shifts the complexity into the boundary conditions of the problem. Since the ψ has to be

periodic, the u will have to be periodic up to a specific phase:

$$\begin{aligned} \psi(-\pi) = \psi(\pi) \quad &\Rightarrow \quad u(\pi)e^{i\pi n_g} = u(a)e^{-i\pi n_g} \\ \psi'(-\pi) = \psi'(\pi) \quad &\Rightarrow \quad \left[u'(-\pi) - in_g u(-\pi)\right] e^{i\pi n_g} = \left[u'(\pi) - in_g u(\pi)\right] e^{-i\pi n_g} \end{aligned}$$

Only in cases where we expect the boundary conditions to be irrelevant then, can we transform away the offset charge. In the case of an extremely deep potential (large E_J/E_C), the lowest states should be localized at the bottom of the well, and the wavefunction should have exponentially small amplitude near $\delta = \pm\pi$, so any effect that the boundary conditions have on the energy levels should be exponentially suppressed.

C.3 Duffing Oscillator

Starting from the Hamiltonian in the phase representation, Eq. C.2, we take the limit of large E_J/E_C, noting that the potential will be deep at $\delta = 0$ and the low-lying states should be well-localized therein. Therefore, we can (1) transform away the offset charge as argued in the previous section, and (2) Taylor expand the cosine. We will keep up to fourth-order in δ so as to capture the leading anharmonicity.

$$\mathcal{H} = -4E_C \frac{\partial^2}{\partial \delta^2} - E_J + \frac{E_J}{2}\delta^2 - \frac{E_J}{24}\delta^4$$

This is the Duffing (quartic) oscillator. Rewriting it in terms of the harmonic oscillator creation and annihilation operators:

$$\mathcal{H} = \sqrt{8E_C E_J}\left(b^\dagger b + \frac{1}{2}\right) - \frac{E_C}{12}\left(b + b^\dagger\right)^4 - E_J$$

Since E_C is small, the unperturbed energies are the harmonic oscillator ladder (minus a constant)

$$E_j^{(0)} = \sqrt{8E_C E_J}\left(j + \frac{1}{2}\right) - E_J$$

And taking perturbation theory to first order, we find the corrections to the energy levels

$$E_j^{(1)} = -\frac{E_C}{12}\langle j|\left(b+b^\dagger\right)^4|j\rangle = -\frac{E_C}{12}(6j^2+6j+3)$$

C.3.1 Relative Anharmonicity

Evaluating the first transition E_{01} and the second transition E_{12}:

$$E_{01} = \sqrt{8E_CE_J} - E_C, \quad E_{12} = \sqrt{8E_CE_J} - 2E_C$$

We find that there is a relative anharmonicity of

$$\frac{E_{12}-E_{01}}{E_{01}} \approx -(8E_J/E_C)^{-1/2}$$

This agrees with [4].

C.3.2 Number operator matrix elements

The matrix elements of the number operator will be useful in the discussion of coupling, and, to lowest-order in E_J/E_C, they can be evaluated without even including the perturbation [4], because the main E_J/E_C dependence enters when writing the number operator the standard way in terms of the ladder operators. Thus, in the large E_J/E_C limit, we have

For diagonal elements:

$$|\langle j|n|j\rangle| = \left|-i\left(\frac{E_J}{32E_C}\right)^{1/4}\langle j|(b-b^\dagger)|j\rangle\right| = 0$$

For eigenstates separated by $k > 1$:

$$|\langle j+k|n|j\rangle| = \left|-i\left(\frac{E_J}{32E_C}\right)^{1/4}\langle j+k|(b-b^\dagger)|j\rangle\right| = 0$$

For neighboring eigenstates:

$$|\langle j+1|n|j\rangle| = \left| -i \left(\frac{E_J}{32E_C}\right)^{1/4} \langle j+1|(b-b^\dagger)|j\rangle \right| = \sqrt{j+1} \left(\frac{E_J}{32E_C}\right)^{1/4}$$

Note that the first and third results above apply to the charge-qubit limit as well (if at the sweet spot), as one can easily calculate with the explicit forms of the energy eigenstates there, whereas the third results would become $1/2$ in that limit.

Bibliography

[1] M. Nielsen and I. Chuang, *Quantum Computation and Quantum Information*. Cambridge University Press, 2000.

[2] I. M. Georgescu, S. Ashhab, and F. Nori, "Quantum simulation," Accepted to Rev. Mod. Phys, 17 Sept 2013. arXiv: 1308.6253v2.

[3] M. H. Devoret and R. J. Schoelkopf, "Superconducting circuits for quantum information: an outlook," *Science*, vol. 339, no. 6124, pp. 1169–1174, 2013. DOI: 10.1126/science.1231930. eprint: http://www.sciencemag.org/content/339/6124/1169.full.pdf. [Online]. Available: http://www.sciencemag.org/content/339/6124/1169.abstract.

[4] J. Koch, T. M. Yu, J. Gambetta, A. A. Houck, D. I. Schuster, J. Majer, A. Blais, M. H. Devoret, S. M. Girvin, and R. J. Schoelkopf, "Charge-insensitive qubit design derived from the cooper pair box," *Phys. Rev. A*, vol. 76, p. 042319, 4 Oct. 2007. DOI: 10.1103/PhysRevA.76.042319. [Online]. Available: http://link.aps.org/doi/10.1103/PhysRevA.76.042319.

[5] J. Majer, J. M. Chow, J. M. Gambetta, J. Koch, B. R. Johnson, J. A. Schreier, L. Frunzio, D. I. Schuster, A. A. Houck, A. Wallraff, A. Blais, M. H. Devoret, S. M. Girvin, and R. J. Schoelkopf, "Coupling superconducting qubits via a cavity bus," *Nature*, vol. 449, no. 7161, pp. 443–447, Sep. 27, 2007, ISSN: 0028-0836. DOI: 10.1038/nature06184. [Online]. Available: http://dx.doi.org/10.1038/nature06184.

[6] L. DiCarlo, J. M. Chow, J. M. Gambetta, L. S. Bishop, B. R. Johnson, D. I. Schuster, J. Majer, A. Blais, L. Frunzio, S. M. Girvin, and R. J. Schoelkopf, "Demonstration of two-qubit algorithms with a superconducting quantum processor," *Nature*, vol. 460, no. 7252, pp. 240–244, Jul. 9, 2009, ISSN: 0028-0836. DOI: 10.1038/nature08121. [Online]. Available: http://dx.doi.org/10.1038/nature08121.

[7] Z. Leghtas, G. Kirchmair, B. Vlastakis, R. J. Schoelkopf, M. H. Devoret, and M. Mirrahimi, "Hardware-efficient autonomous quantum memory protection," *Phys. Rev. Lett.*, vol. 111, p. 120501, Sep. 2013. DOI: 10.1103/PhysRevLett.111.120501. [Online]. Available: http://link.aps.org/doi/10.1103/PhysRevLett.111.120501.

[8] A. A. Abdumalikov Jr, J. M. Fink, K. Juliusson, M. Pechal, S. Berger, A. Wallraff, and S. Filipp, "Experimental realization of non-abelian non-adiabatic geometric gates," *Nature*, vol. 496, no. 7446, pp. 482–485, Apr. 25, 2013, Letter, ISSN: 0028-0836. [Online]. Available: http://dx.doi.org/10.1038/nature12010.

[9] M. Neeley, M. Ansmann, R. C. Bialczak, M. Hofheinz, E. Lucero, A. D. O'Connell, D. Sank, H. Wang, J. Wenner, A. N. Cleland, M. R. Geller, and J. M. Martinis, "Emulation of a quantum spin with a superconducting phase qudit," *Science*, vol. 325, no. 5941, pp. 722–725, 2009. DOI: 10.1126/science.1173440. eprint: http://www.sciencemag.org/content/325/5941/722.full.pdf. [Online]. Available: http://www.sciencemag.org/content/325/5941/722.abstract.

[10] B. P. Lanyon, T. J. Weinhold, N. K. Langford, J. L. O'Brien, K. J. Resch, A. Gilchrist, and A. G. White, "Manipulating biphotonic qutrits," *Phys. Rev. Lett.*, vol. 100, p. 060504, 6 Feb. 2008. DOI: 10.1103/PhysRevLett.100.060504. [Online]. Available: http://link.aps.org/doi/10.1103/PhysRevLett.100.060504.

[11] T. P. Orlando and K. A. Delin, *Foundations of Applied Superconductivity*. Addison-Wesley Publishing Company, 1991.

[12] V. Bouchiat, D. Vion, P. Joyez, D. Esteve, and M. H. Devoret, "Quantum coherence with a single cooper pair," *Physica Scripta*, vol. 1998, no. T76, p. 165, 1998. [Online]. Available: http://stacks.iop.org/1402-4896/1998/i=T76/a=024.

[13] T. Duty, D. Gunnarsson, K. Bladh, and P. Delsing, "Coherent dynamics of a josephson charge qubit," *Phys. Rev. B*, vol. 69, p. 140 503, 14 Apr. 2004. DOI: 10.1103/PhysRevB.69.140503. [Online]. Available: http://link.aps.org/doi/10.1103/PhysRevB.69.140503.

[14] D. Vion, A. Aassime, A. Cottet, P. Joyez, H. Pothier, C. Urbina, D. Esteve, and M. H. Devoret, "New directions in mesoscopic physics (towards nanoscience)," in. Springer Netherlands, 2003, ch. Superconducting quantum bit based on the Cooper pair box.

[15] M. H. Devoret, A. Wallraff, and J. M. Martinis, "Superconducting qubits: a short review," arXiv:cond-mat/0411174.

[16] T. Duty, G. Johansson, K. Bladh, D. Gunnarsson, C. Wilson, and P. Delsing, "Observation of quantum capacitance in the cooper-pair transistor," *Phys. Rev. Lett.*, vol. 95, p. 206 807, 20 Nov. 2005. DOI: 10.1103/PhysRevLett.95.206807. [Online]. Available: http://link.aps.org/doi/10.1103/PhysRevLett.95.206807.

[17] A. Blais, J. Gambetta, A. Wallraff, D. I. Schuster, S. M. Girvin, M. H. Devoret, and R. J. Schoelkopf, "Quantum-information processing with circuit quantum electrodynamics," *Phys. Rev. A*, vol. 75, p. 032 329, 3 Mar. 2007. DOI: 10.1103/PhysRevA.75.032329. [Online]. Available: http://link.aps.org/doi/10.1103/PhysRevA.75.032329.

[18] J. Q. You and F. Nori, "Superconducting circuits and quantum information," *Physics Today*, vol. 58, p. 42, 11 2005. DOI: 10.1063/1.2155757.

[19] A. Blais, R.-S. Huang, A. Wallraff, S. M. Girvin, and R. J. Schoelkopf, "Cavity quantum electrodynamics for superconducting electrical circuits: an architecture for quantum computation," *Phys. Rev. A*, vol. 69, p. 062 320, 6 Jun. 2004. DOI: 10.1103/PhysRevA.

69.062320. [Online]. Available: http://link.aps.org/doi/10.1103/PhysRevA.69.062320.

[20] D. A. Steck, *Quantum and Atom Optics*. Dec. 6, 2011. [Online]. Available: http://steck.us/teaching.

[21] H. Walther, B. T. H. Varcoe, B.-G. Englert, and T. Becker, "Cavity quantum electrodynamics," *Reports on Progress in Physics*, vol. 69, no. 5, p. 1325, 2006. [Online]. Available: http://stacks.iop.org/0034-4885/69/i=5/a=R02.

[22] S. Richer, "Perturbative analysis of two-qubit gates on transmon qubits," Master's thesis, RWTH Aachen University, Sep. 2013. [Online]. Available: http://www.physik.rwth-aachen.de/fileadmin/user_upload/www_physik/Institute/Inst_QI/Theses/master/master_richter2013.pdf.

[23] S. Haroche and D. Kleppner, "Cavity quantum electrodynamics," *Physics Today*, vol. 42, p. 24, 1 1989. DOI: http://dx.doi.org/10.1063/1.881201.

[24] D. Kleppner, "Inhibited spontaneous emission," *Phys. Rev. Lett.*, vol. 47, pp. 233–236, 4 Jul. 1981. DOI: 10.1103/PhysRevLett.47.233. [Online]. Available: http://link.aps.org/doi/10.1103/PhysRevLett.47.233.

[25] M. Scully and M. S. Zubairy, *Quantum Optics*. Cambridge University Press, 1997.

[26] C. Rigetti, J. M. Gambetta, S. Poletto, B. L. T. Plourde, J. M. Chow, A. D. Córcoles, J. A. Smolin, S. T. Merkel, J. R. Rozen, G. A. Keefe, M. B. Rothwell, M. B. Ketchen, and M. Steffen, "Superconducting qubit in a waveguide cavity with a coherence time approaching 0.1 ms," *Phys. Rev. B*, vol. 86, p. 100506, 10 Sep. 2012. DOI: 10.1103/PhysRevB.86.100506. [Online]. Available: http://link.aps.org/doi/10.1103/PhysRevB.86.100506.

[27] J. M. Chow, L. DiCarlo, J. M. Gambetta, F. Motzoi, L. Frunzio, S. M. Girvin, and R. J. Schoelkopf, "Optimized driving of superconducting artificial atoms for improved single-qubit gates," *Phys. Rev. A*, vol. 82, p. 040305, 4 Oct. 2010. DOI: 10.1103/

PhysRevA.82.040305. [Online]. Available: http://link.aps.org/doi/10.1103/PhysRevA.82.040305.

[28] M. H. Devoret, *Quantum Fluctuations: Les Houches Session LXIII.* Elsevier, 1997, ch. Quantum Fluctuations in Electrical Circuits.

[29] A. Wallraff, *A charge qubit: the cooper pair box*, Quantum Systems for Information Technology. [Online]. Available: http://qudev.phys.ethz.ch/content/courses/QSIT10/QSIT10_V07_slides.pdf.